

Discovery of two warm mini-Neptunes with contrasting densities orbiting the young K3V star TOI-815*

Angelica Psaridi¹, Hugh Osborn^{2,3}, François Bouchy¹, Monika Lendl¹, Léna Parc¹, Nicolas Billot¹, Christopher Broeg^{2,4}, Sérgio G. Sousa⁵, Vardan Adibekyan^{5,6}, Omar Attia¹, Andrea Bonfanti⁷, Hritam Chakraborty¹, Karen A. Collins⁸, Jeanne Davoult², Elisa Delgado-Mena⁵, Nolan Grieves¹, Tristan Guillot⁹, Alexis Heitzmann¹, Ravit Helled¹⁰, Coel Hellier¹¹, Jon M. Jenkins¹³, Henrik Knierim¹⁰, Andreas Krenn⁷, Jack J. Lissauer¹³, Rafael Luque¹², David Rapetti^{13,14}, Nuno C. Santos^{5,6}, Olga Suárez⁹, Julia Venturini¹, Francis P. Wilkin¹⁵, Thomas G. Wilson¹⁶, Joshua N. Winn¹⁷, Carl Ziegler¹⁸, Tiziano Zingales^{19,20}, Yann Alibert^{2,4}, Alexis Brandeker²¹, Jo Ann Egger⁴, Davide Gandolfi²², Matthew J. Hooton²³, Amy Tuson²⁴, Solène Ulmer-Moll^{1,4}, Lyu Abe⁹, Romain Allart²⁴, Roi Alonso^{25,26}, David R. Anderson¹⁶, Guillem Anglada^{27,28}, Tamas Bárczy²⁹, David Barrado³⁰, Susana C. C. Barros^{5,6}, Wolfgang Baumjohann⁷, Mathias Beck¹, Thomas Beck⁴, Willy Benz^{4,2}, Xavier Bonfils³¹, Luca Borsato²⁰, Vincent Bourrier¹, David R. Ciardi³², Andrew Collier Cameron³³, Sébastien Charnoz³⁴, Marion Cointepas^{1,31}, Szilárd Csizmadia³⁵, Patricio Cubillos^{20,7}, Gaspare Lo Curto³⁶, Melvyn B. Davies³⁷, Tansu Daylan³⁸, Magali Deleuil³⁹, Adrien Deline¹, Laetitia Delrez^{40,41}, Olivier D. S. Demangeon⁵, Brice-Olivier Demory^{2,4}, Caroline Dorn⁴², Xavier Dumusque¹, David Ehrenreich¹, Anders Erikson³⁵, Alain Lecavelier des Etangs⁴³, Elena Diana de Miguel Ferreras⁴⁴, Andrea Fortier^{4,2}, Luca Fossati⁷, Yolanda G. C. Frensch¹, Malcolm Fridlund^{45,46}, Michaël Gillon⁴⁰, Manuel Güdel⁴⁷, Maximilian N. Günther⁴⁸, Janis Hagelberg¹, Christiane Helling^{7,49}, Sergio Hoyer³⁹, Kate G. Isaak⁴⁸, Laszlo L. Kiss^{50,51}, Kristine Lam³⁵, Jacques Laskar⁵², Baptiste Lavie¹, Christophe Lovis¹, Demetrio Magrin²⁰, Luca Marafatto²⁰, Pierre Maxted¹¹, Scott McDermott⁵³, Djamel Mékarnia⁹, Christoph Mordasini^{4,2}, Felipe Murgas²⁶, Valerio Nascimbeni²⁰, Louise D. Nielsen⁵⁴, Göran Olofsson²¹, Roland Ottensamer⁴⁷, Isabella Pagano⁵⁵, Enric Pallé^{25,26}, Gisbert Peter³⁵, Giampaolo Piotto^{20,19}, Don Pollacco¹⁶, Didier Queloz^{42,23}, Roberto Ragazzoni^{20,19}, Devin Ramos¹⁵, Nicola Rando⁴⁸, Heike Rauer^{35,56,57}, Christian Reimers⁴⁷, Ignasi Ribas^{27,28}, Sara Seager^{3,58,59}, Damien Ségransan¹, Gaetano Scandariato⁵⁵, Attila Simon^{4,2}, Alexis M. S. Smith³⁵, Manu Stalport^{41,40}, Manfred Steller⁷, Gyula Szabó^{60,61}, Nicolas Thomas⁴, Tyler A. Pritchard⁶², Stéphane Udry¹, Carlos Corral Van Damme⁴⁸, Valérie Van Grootel⁴¹, Eva Villaver^{25,26}, Ingo Walter³⁵, Nicholas Walton²⁴, Cristilyn N. Watkins⁸, Richard G. West^{16,63}

(Affiliations can be found after the references)

ABSTRACT

We present the discovery and characterization of two warm mini-Neptunes transiting the K3V star TOI-815 in a K-M binary system. Analysis of the spectra and rotation period reveal it to be a young star with an age of 200^{+400}_{-200} Myr. TOI-815b has a 11.2-day period and a radius of $2.94 \pm 0.05 R_{\oplus}$ with transits observed by TESS, CHEOPS, ASTEP, and LCOGT. The outer planet, TOI-815c, has a radius of $2.62 \pm 0.10 R_{\oplus}$, based on observations of three non-consecutive transits with TESS, while targeted CHEOPS photometry and radial velocity follow-up with ESPRESSO were required to confirm the 35-day period. ESPRESSO confirmed the planetary nature of both planets and measured masses of $7.6 \pm 1.5 M_{\oplus}$ ($\rho_p = 1.64^{+0.33}_{-0.31} \text{ g cm}^{-3}$) and $23.5 \pm 2.4 M_{\oplus}$ ($\rho_p = 7.2^{+1.1}_{-1.0} \text{ g cm}^{-3}$) respectively. Thus, the planets have very different masses, unlike the usual similarity of masses in compact multi-planet systems. Moreover, our statistical analysis of mini-Neptunes orbiting FGK stars suggests that weakly irradiated planets tend to have higher bulk densities compared to those suffering strong irradiation. This could be ascribed to their cooler atmospheres, which are more compressed and denser. Internal structure modeling of TOI-815b suggests it likely has a H-He atmosphere constituting a few percent of the total planet mass, or higher if the planet is assumed to have no water. In contrast, the measured mass and radius of TOI-815c can be explained without invoking any atmosphere, challenging planetary formation theories. Finally, we infer from our measurements that the star is viewed close to pole-on, which implies a spin-orbit misalignment at the 3σ level. This result emphasizes the peculiarity of the system's orbital architecture, and probably hints at an eventful past dynamical history.

Key words. planets and satellites: detection – planets and satellites: composition - planets and satellites: formation - techniques: photometry – techniques: radial velocities

* This study uses TESS data, CHEOPS data observed as part of Guaranteed Time Observation (GTO) programs CH_PR10031 and CH_PR10048 and ESPRESSO data collected with the ESO-3.6 m

under programs 105.20P7.001, 109.23DX.001 and 110.2481.001 (PI: Bouchy). The photometric and radial velocity data in this work are only available in electronic form at the CDS via anonymous ftp to cdsarc.u-

1. Introduction

The Transiting Exoplanet Survey Satellite (TESS; Ricker et al. 2015) and the Kepler space mission have profoundly transformed our understanding of planets by detecting thousands of exoplanets using the transit method, particularly those with radii below $4 R_{\oplus}$ and relatively short orbital periods. Fulton et al. (2017), using precise planet radius measurements, identified a clear bimodal distribution in the radii of small-sized planets. It appears that close-orbiting planets predominantly fall into two categories: super-Earths (below $1.8 R_{\oplus}$) or sub-Neptunes (2 to $4 R_{\oplus}$), with very few planets occupying the intermediate range (the so-called radius valley). Four mechanisms have been proposed to explain the origin of the two populations of super-Earths and sub-Neptunes: photo-evaporation of the H-He envelopes due to high-energy radiation from the host star (Lopez & Fortney 2013; Owen & Wu 2017; Jin & Mordasini 2018; Rogers & Owen 2021; Attia et al. 2021), atmospheric mass-loss fueled by the cooling luminosity of a planet's core (Ginzburg et al. 2018; Gupta & Schlichting 2019), a combination of ex-situ formation and photo-evaporation (Venturini et al. 2020), and an in-situ gas-poor formation scenario (Lee et al. 2022). These mechanisms predict different compositions for the mini-Neptunes, ranging from dry planets composed of a H/He envelope atop a rocky core (Owen & Wu 2017; Jin & Mordasini 2018; Gupta & Schlichting 2019; Lee et al. 2022) to water-worlds with a thin or without any H/He atmosphere (Venturini et al. 2020). The mechanisms predict as well distinct relationships between stellar and planetary mass, as well as differing locations (in the period-radius-mass space) of the valley and varying occurrence rates relative to the age of the systems (Berger et al. 2020; Petigura et al. 2022).

Numerous ongoing follow-up programs are dedicated to characterizing the masses of super-Earth and mini-Neptune-sized planets located close to the 'radius valley' of short-period orbits. However, there is limited coverage of mini-Neptune-sized planets with low stellar irradiation (less than $30 S_{\oplus}$) and long orbital periods (greater than 15 days). We started a radial velocity (RV) follow-up campaign with ESPRESSO dedicated to the characterization and precise density measurement of warm mini-Neptune planets that transit FGK dwarfs. Currently, there are 17 exoplanets in this parameter range with stars brighter than $V=12$ and well-constrained densities¹ according to the Planets catalog² (Otegi et al. 2020).

Multi-planet systems provide the opportunity to study and make comparisons among planets of different densities and compositions within a single system. One observed trend in the diversity of planetary systems is that planets seem to resemble "peas in the pod", i.e. multi-transiting systems tend to have planets with similar sizes and geometrically spaced orbital distances (Weiss et al. 2018; Otegi et al. 2022; Mishra et al. 2023). Understanding these trends is crucial since they can elucidate underlying physical processes and constrain formation theories.

In this work, we present the discovery of two mini-Neptune planets transiting TOI-815, a $V=11.2$ mag, K3V star. The innermost planet, designated as TOI-815b, has an orbital period of 11.2 days. This planet's transits were captured by TESS during Sector 6, 36 and 63, as well as by the Characterising ExOPlanet Satellite (CHEOPS; Benz et al. 2021), Antarc-

strasbg.fr (130.79.128.5) or via <http://cdsarc.u-strasbg.fr/viz-bin/qcat?J/A+A/>

¹ $\sigma_M/M \leq 25\%$ and $\sigma_R/R \leq 8\%$

²Available on the Data & Analysis Center for Exoplanets (DACE) platform (<https://dace.unige.ch>)

tic Search for Transiting ExoPlanets telescope (ASTEP; Guillot et al. 2015), and Las Cumbres Observatory Global Telescope (LCOGT; Brown et al. 2013). As for the outer planet, TOI-815c, TESS detected three transits during the aforementioned sectors, however a unique period could not be delivered. Additionally, targeted CHEOPS photometry was performed in order to investigate potential period aliases, leading to the confirmation of a 35-day orbital period for TOI-815c. The planetary nature of both objects has been confirmed with RV follow-up using ESPRESSO (Pepe et al. 2021).

The paper is structured as follows: In Section 2, we provide a detailed description of the space- and ground-based observations with TESS, CHEOPS, ASTEP, LCOGT, as well as the ESPRESSO RV observations. Section 3 details the determination of the host star parameters by combining high-resolution spectra. In Section 4, we present our global photometric and RV analysis and its results. Finally, in Section 5, we present a discussion of the system and conclude in Section 6.

2. Observations

2.1. TOI-815 in a binary system

Behmard et al. (2022) searched for stellar companions to TESS Objects of Interest (TOI; Guerrero et al. 2021) by cross-matching them with the Gaia Early Data Release 3 catalog (EDR3). TOI-815 was identified to be in a binary system with the nearest known neighbor in the TICv8 catalog (Stassun et al. 2019), TIC 102840237 (GAIA DR3 5415648821874435584) that is located approximately 359 AU ($\sim 6.4'$) north of TOI-815 (Figure 1). According to the TICv8 catalog, TIC 102840237 is an M-dwarf with $T_{\text{eff}} = 3766 \pm 157$ K and is 2.5 magnitudes dimmer than TOI-815 in the G band. To compensate for flux contamination in the photometry, we included a dilution factor for the light curves, as presented below.

2.2. TESS photometry

The TOI-815 system (TIC 102840239) was observed in TESS Sector 9 (2018 December 12 to 2019 January 06) in 30-minute cadence and Sectors 36 (2021 March 07 to 2021 April 01) and 63 (2023 March 10 to 2023 April 06) in 20-second cadence. In Sectors 9 and 36, the target was imaged on CCD 2 of camera 2, and in Sector 63, on CCD 1 of camera 2. The 30-minute Full Frame Image (FFI) light curves were extracted by the MIT Quick Look Pipeline (QLP; Huang et al. 2020), resulting in the Simple Aperture Photometry (SAP) flux and the QLP Kepler Spline SAP (KSPSAP, Vanderburg & Johnson 2014) flux. The 2-minute and 20-second cadence photometry was produced by the Science Processing Operations Center (SPOC; Jenkins et al. 2016) pipeline at the NASA Ames Research Center, resulting in the SAP (Twicken et al. 2010; Morris et al. 2020) flux and the Presearch Data Conditioning SAP (PDCSAP; Smith et al. 2012; Stumpe et al. 2012, 2014) flux.

On 2019 June 21, the TESS data public website³ announced the discovery of a 11.2-day TESS Object of Interest (TOI; Guerrero et al. 2021), TOI-815b. The SPOC detected the transit signature of TOI-815b in searches of Sector 36, and a search of Sector 36 and 63 with a noise-compensating matched filter (Jenkins 2002, 2010, 2020), and the signature was fitted with an initial limb-darkened transit model (Li et al. 2019) and passed all the diagnostic tests presented in the Data Validation report (Twicken

³<https://tev.mit.edu/data/>

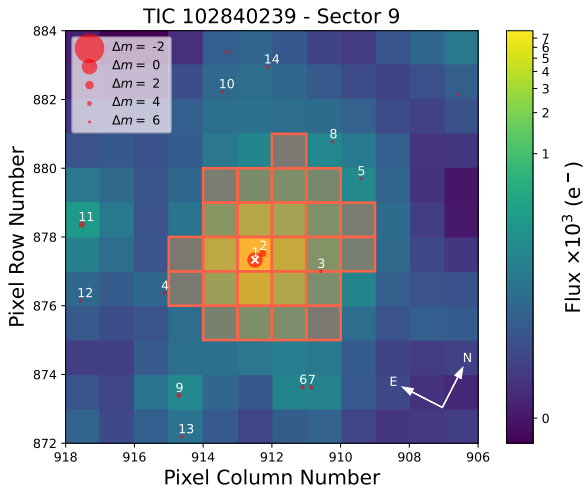


Fig. 1: TESS Target Pixel File (TPF) of TOI-815 created with `tpfplotter` (Aller et al. 2020). The orange pixels define the aperture mask utilized for extracting the photometry. Additionally, the red circles indicate neighboring objects from the Gaia DR2 catalog, with the circle size corresponding to the brightness difference compared to the targets (as indicated in the legend). Our target is marked with a white cross. Pixel scale is 21''/pixel.

et al. 2018). In particular, the difference image centroiding test for the multisector search located the host star within 1.4 ± 3.4 arcsec of the transit source. Seven transits with a depth of 1301 ± 54 ppm and a duration of 3.06 ± 0.43 hours were identified in Sectors 9, 36 and 63 (Figure A.1). However, TOI-815 showed one additional transit in each Sector with a transit depth of 1004 ± 73 ppm and a duration of 2.53 ± 0.59 hours, suggesting a second transiting companion. As presented in this work, with follow-up observations using ESPRESSO and CHEOPS, we confirmed the planetary nature and characterized the second planet.

For the analysis of the 30-minute cadence data we used the KSPSAP flux. For the 2-minute and 20-second cadence light curves, we used the uncorrected SAP flux and accounted for the systematic noise with the `juliet` package (Espinoza et al. 2019) using Gaussian Process (GP) models with an approximate Matérn-3/2 kernel.

In order to check the existence of contaminant sources, we plotted the target pixel file (TPF, Figure 1) along with the aperture mask used for the SAP flux. The plot was generated using `tpfplotter` (Aller et al. 2020). The apertures used for extracting the light curves in all three Sectors were contaminated by TIC 102840237 (Section 2.1) and therefore we included a dilution coefficient during the modeling of the TESS light curves. Our TESS light curve analysis is described in more detail in Section 4.4.

2.3. CHEOPS observations

CHEOPS is a 32 cm aperture ESA telescope dedicated to the characterisation of transiting exoplanets. It performs high-precision photometry in a broad optical passband (330 to 1100 nm). The instrument is optimised for bright stars, making it an ideal facility to observe small-amplitude transits created by low-mass planets (e.g., Delrez et al. 2021; Leleu et al. 2021), or characterise the minute emission signals of hot Jupiters at optical wavelengths (Lendl et al. 2020; Krenn et al. 2023). Among vari-

ous scientific goals, the CHEOPS space mission is also suited to improve the radius precision of known exoplanets discovered by TESS (Bonfanti et al. 2021a) by observing additional transits and to recover the true period of double transit candidates detected by TESS (e.g., Osborn et al. 2023; Ulmer-Moll et al. 2023; Garai et al. 2023). TOI-815 was jointly observed by two programs within the CHEOPS Guaranteed Time Observing (GTO): one targeting improved radius precision for multi-planet systems detected by NASA TESS (CHESS; PR0031) and the other targeted on confirming the orbital periods of long-period candidates found by TESS (DUOS; PR0048). The observations had an exposure time of 60 s, typical duration of 5-7 orbits (8.2-11.4 hours), and achieved efficiencies between 51 and 73% (e.g. due to Earth occultations, Earth's stray light contamination and South Atlantic Anomaly crossings). CHEOPS data are automatically processed with an automatic aperture photometry pipeline (Hoyer et al. 2020). We however re-extracted the photometry using Point Spread Function (PSF) photometry with the PIPE package⁴ (Brandeker et al. 2022) which, due to the large asymmetric PSF of CHEOPS, typically results in photometry with less influenced by external factors such as companion stars, roll-angle trends, etc. PIPE takes into account the flux contamination from nearby stars by subtracting a synthetic image using the PSF and GAIA DR2 parameters for the neighbor stars. Therefore, the dilution factor for the CHEOPS light curves was fixed to one.

2.4. Ground-based photometry

The TESS pixel scale is $\sim 21''$ pixel $^{-1}$ and photometric apertures typically extend out to roughly 1', generally causing multiple stars to blend in the TESS aperture. To determine the true source of transit signals in the TESS data, improve the transit ephemerides, and check the SPOC pipeline transit depth after accounting for the crowding metric, we conducted photometric ground-based follow-up observations with ASTEP and LCOGT of the field around TOI-815 as part of the TESS Follow-up Observing Program⁵ Sub Group 1 (TFOP; Collins 2019). We used the TESS Transit Finder, which is a customized version of the Tapir software package (Jensen 2013), to schedule our transit sit observations.

2.4.1. ASTEP

We observed TOI-815 with ASTEP on 2021 April 04 but could only rule-out an ingress of TOI-815b which was, at the time, predicted to occur at BJD 2459309.02. Subsequent analysis (see Section 5.5) shows that as a result of TTVs, the prediction was incorrect, and that the ingress should have started at 2459309.93 ± 0.0285 , later than the end of this first series of observations. On 2022 September 13, using an improved camera system (Dransfield et al. 2022; Schmider et al. 2022) we observed the target again (Figure 2), with 15 second exposures, at wavelengths ranging from about 700 to 1000 nm (Schmider et al. 2022). The data were processed on site with an IDL-based aperture photometry pipeline (Abe et al. 2013; Mékarnia et al. 2016). We detected an on-time 2.0 ppt transit of TOI-815b, using a 13.9 arcsec target aperture. While the ingress was clearly evident, the egress was affected by sky brightening, with a Sun at about 12° below the horizon at end of the observation sequence.

⁴<https://github.com/alphapsa/pipe>

⁵<https://tess.mit.edu/followup/>

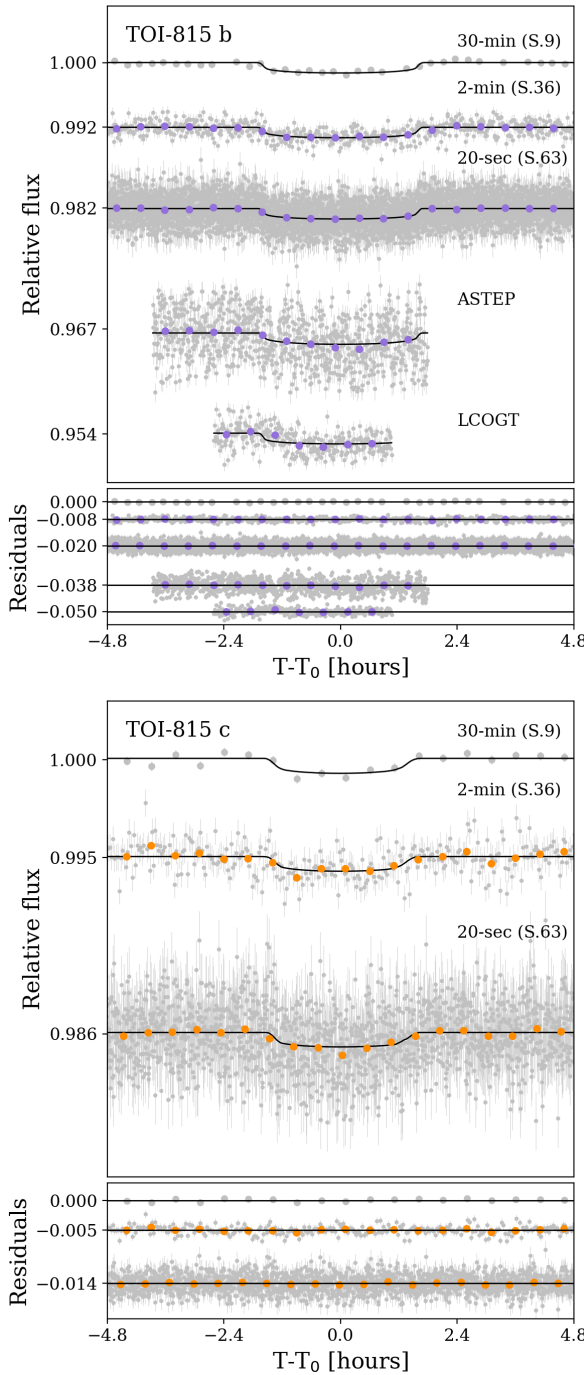


Fig. 2: Phase-folded TESS, ASTEP and LCOGT light curves of TOI-815b (top panel) and TESS light curves of TOI-815c (bottom panel). The data are binned to 30 minutes (purple and orange circles).

2.4.2. LCOGT

We observed an intended full transit window of TOI-815b on 2021 February 18 (Figure 2) in Pan-STARRS z -short band using the LCOGT 1.0 m network node at South Africa Astronomical Observatory (SAAO). However, after updating the ephemeris from TESS Sector 36 data, we determined that the follow-up observations were out of transit by approximately one day. Therefore these data are not considered further in this work. We observed a partial transit window of TOI-815b on 2023 March 11

using the same band-pass and LCOGT network node. The images were calibrated by the standard LCOGT BANZAI pipeline (McCully et al. 2018) and differential photometric data were extracted using AstroImageJ (Collins et al. 2017). We used circular photometric apertures with radius $3''.9$. The target star aperture was diluted by 0.85% by the neighbor star (Section 2.1). The best zero, one, or two detrending vectors were retained if they decreased the Bayesian Information Criterion (BIC) for a fit by at least two per detrend parameter. We found that a proxy for sky transparency and the Y-centroid of the target star on the detector detrending pair provided the best improvement to the light curve fit that was justified by the BIC values.

2.5. Spectroscopic follow-up with ESPRESSO

We acquired 34 high-resolution spectroscopic observations of TOI-815 using ESPRESSO on the 8.2 m Very Large Telescope (VLT) located in Paranal, Chile. The observations were carried out between 2021 April 04 and 2022 December 04 as part of the observing programs 105.20P7.001, 109.23DX.001 and 110.2481.001 (PI: Bouchy), dedicated to the characterization of warm mini-Neptune transiting exoplanets. The observations have an integration time ranging from 600 to 700 s, a median resolving power of 140,000 using 2×1 binning, and a wavelength range of 380–788 nm. The RVs and activity indicators were extracted using version 3.0.0 of the ESPRESSO pipeline, and we computed the RVs by cross-correlating the Echelle spectra with a G2 numerical mask.

The ESPRESSO pipeline was devised to correct the residual atmosphere dispersion, i.e., after Atmospheric Dispersion Corrector (ADC) correction. This reduces significantly the chromatic effects on the data. Out of the total observations, six were identified as unreliable since the flux correction was not applied and therefore were excluded from the global modeling. The average uncertainty of the RV data is 0.68 m s^{-1} and the RMS is 0.74 m s^{-1} . We report the ESPRESSO RV measurements and their uncertainties, along with the FWHM, bisector, contrast, S-index and $\text{H}\alpha$ -index in Table B.1. The excluded data points are noted in the same Table. The RV time series and the phase-folded RVs for TOI-815b and TOI-815c are shown in Figure 3.

2.6. High resolution imaging

High-angular resolution imaging is needed to search for nearby sources that can contaminate the TESS photometry, resulting in an underestimated planetary radius, or be the source of astrophysical false positives, such as background eclipsing binaries. We searched for stellar companions to TOI-815 with speckle imaging on the 4.1-m Southern Astrophysical Research (SOAR) telescope (Tokovinin 2018) on 2019 July 14, observing in Cousins I-band, a similar visible band-pass as TESS. This observation was sensitive to a 5.8-magnitude fainter star at an angular distance of 1 arcsec from the target. More details of the observations within the SOAR TESS survey are available in Ziegler et al. (2020). The 5σ detection sensitivity and speckle auto-correlation functions from the observations are shown in Figure 4. No nearby stars were detected within $3''$ of TOI-815 in the SOAR observations. The binary star mentioned in Section 2.1 has a separation of $6''.4$, which places it outside SOAR's field of view, and as a result, it was not detected.

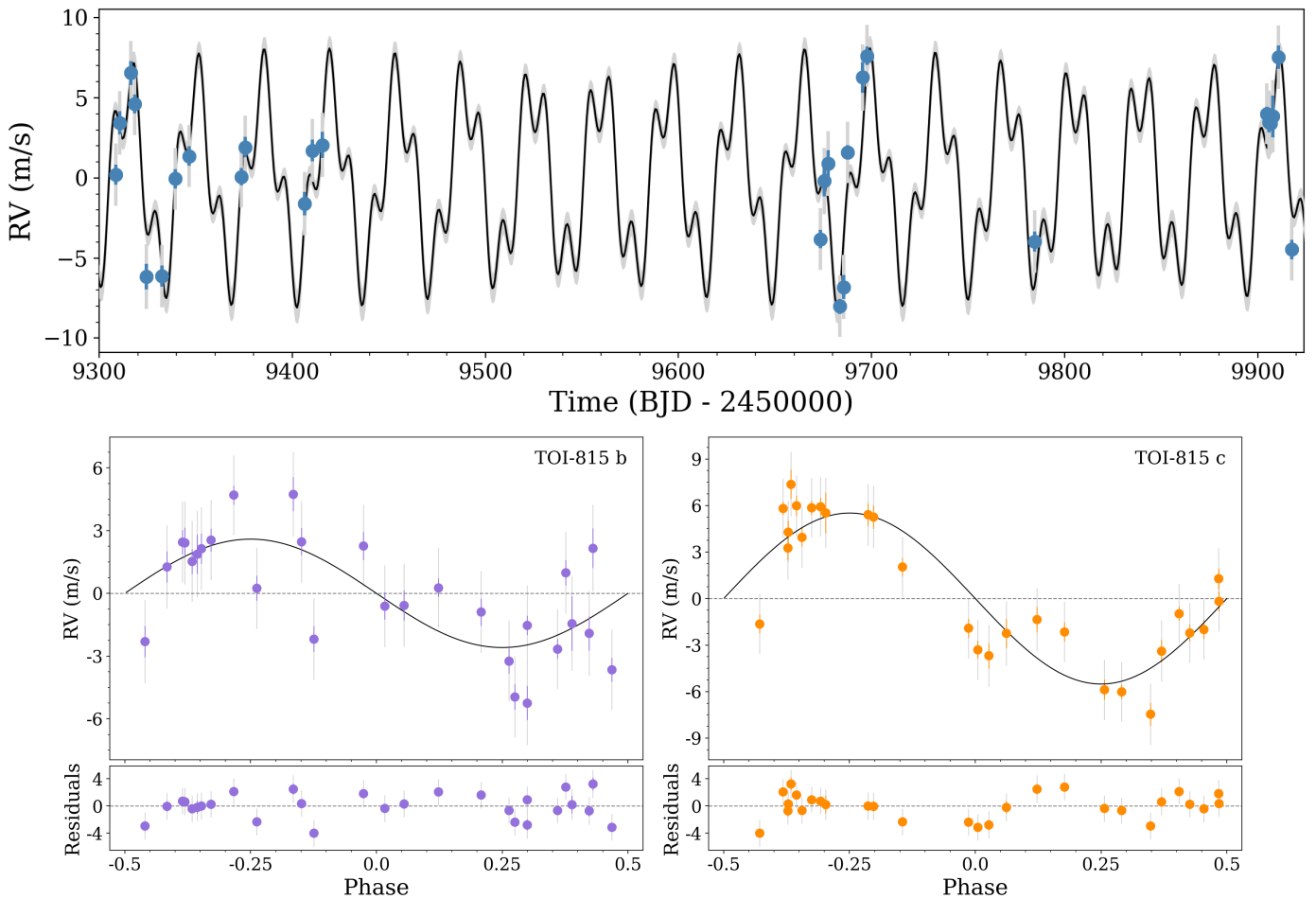


Fig. 3: Relative RV measurements with ESPRESSO and best-fit models for TOI-815. *Top*: Time series of ESPRESSO RV measurements are displayed in blue. The complete inferred model, comprising signals from two planets along with the activity-induced signal, is represented by a continuous solid line. *Bottom*: Phase-folded RVs for TOI-815b (left) and TOI-815c (right). In all plots, the error bars in grey account for the estimated jitter ($\sigma_{w,\text{ESPRESSO}}$).

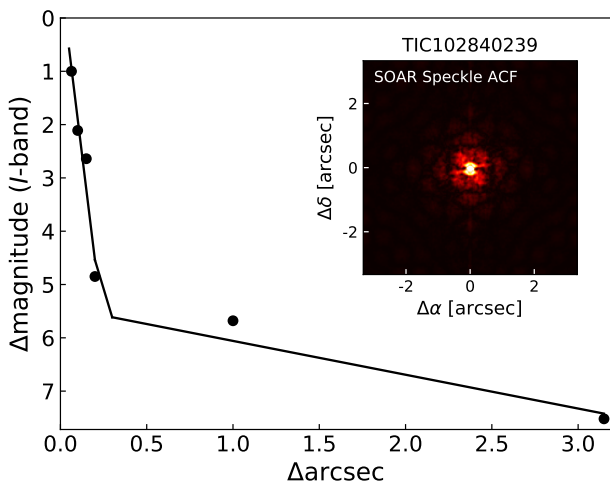


Fig. 4: SOAR speckle imaging (5σ upper limits) of TOI-815 that rules out the presence of stellar companions within a $3''$. The image inset illustrates the speckle auto-correlation function.

3. Stellar characterization

3.1. Spectroscopic parameters

The stellar spectroscopic parameters (T_{eff} , $\log g$, microturbulence, $[\text{Fe}/\text{H}]$) were estimated using the ARES+MOOG methodology. The methodology is described in detail in [Sousa et al. \(2021\)](#); [Sousa \(2014\)](#); [Santos et al. \(2013\)](#); [Sousa et al. \(2008\)](#). For this, we used the latest version of ARES⁷ ([Sousa et al. 2007, 2015](#)) to consistently measure the equivalent widths (EW) of selected iron lines on the combined ESPRESSO spectrum of TOI-815. Because the star has an effective temperature below 5200 K, we use the appropriate list of iron lines presented in [Tsantaki et al. \(2013\)](#). In this analysis we use a minimization process to find the ionization and excitation equilibrium to converge for the best set of spectroscopic parameters. This process makes use of a grid of Kurucz model atmospheres ([Kurucz 1993a](#)) and the radiative transfer code MOOG ([Sneden 1973](#)). We also derived a more accurate trigonometric surface gravity using recent GAIA data following the same procedure as described in [Sousa et al. \(2021\)](#).

Using the stellar atmospheric parameters, we determined the abundances of Mg ($[\text{Mg}/\text{H}] = -0.03 \pm 0.09$ dex) and Si

⁷The last version, ARES v2, can be downloaded at <https://github.com/sousasag/ARES>

$[\text{Si}/\text{H}] = -0.03 \pm 0.06$ dex) closely following the classical curve-of-growth analysis method described in e.g., Adibekyan et al. (2012, 2015). As for the stellar parameter determination, we used ARES to measure the EWs of the spectral lines of these elements, and used a grid of Kurucz model atmospheres (Kurucz 1993a) and the radiative transfer code MOOG (Sneden 1973) to convert the EWs into abundances under assumption of local thermodynamic equilibrium.

Finally, we have estimated the projected rotational velocity, $v \sin i_*$, by performing spectral synthesis around isolated iron lines in the region of Li line at 6708 Å (discussed in Section 3.2). We used the code MOOG and the same model atmosphere used for the abundance determination. The spectral lines are very narrow and despite the very high resolution of ESPRESSO spectra we are only able to set an upper limit of $v \sin i_* < 1 \text{ km s}^{-1}$. All the parameters are presented in Table 1.

3.2. Mass, radius and age

We determined the stellar radius of TOI-815 via a MCMC modified infrared flux method (Blackwell & Shallis 1977; Schanche et al. 2020) by constructing spectral energy distributions (SEDs) using stellar atmospheric models from two catalogues (Kurucz 1993b; Castelli & Kurucz 2003) and the results of our spectral analysis as priors. By comparing synthetic derived from these SEDs and the observed broadband photometry in the following bandpasses: *Gaia* G , G_{BP} , and G_{RP} , 2MASS J , H , and K , and *WISE* $W1$ and $W2$ (Skrutskie et al. 2006; Wright et al. 2010; Gaia Collaboration et al. 2022) we derived the bolometric flux of TOI-815. This is converted into effective temperature and angular diameter that is subsequently combined with the offset-corrected *Gaia* parallax Lindegren et al. (2021) to determine the stellar radius. To allow for model uncertainties to propagate to our stellar radius we used a Bayesian modelling averaging of the radius posterior distributions produced using the aforementioned stellar catalogues.

We determined the stellar mass M_* and age t_* by inputting T_{eff} , $[\text{Fe}/\text{H}]$, and R_* (Table 1) along with their uncertainties in the isochrone placement algorithm (Bonfanti et al. 2015, 2016). Following interpolation of the input parameters within pre-computed grids of PARSEC⁹ v1.2S (Marigo et al. 2017) isochrones and evolutionary tracks, we obtained $M_* = 0.776 \pm 0.036 M_\odot$ and $t_* = 200^{+400}_{-200}$ Myr, where the error bars were computed by adding 4% and 20% in quadrature to the internal uncertainties coming from the interpolation scheme (as justified in Bonfanti et al. 2021a) to account for the isochrone precision. On the one hand, the young age we derived is apparently in disagreement with the low $v \sin i$ value. On the other hand, an older main sequence star would have a smaller stellar radius differing more than 3σ from our R_* estimate.

To further assess the evolutionary stage of the star we have derived the Li abundance by performing a spectral synthesis (Figure C.1) using the same model atmospheres and radiative transfer code as to obtain the spectroscopic parameters and abundances (see Delgado Mena et al. 2014, for further details). We obtain a value of $A(\text{Li})^{10} = 1.15$ dex which is very high for stars of such cool temperature, because their thick convective envelopes allow for the mixing of material to interior regions hot enough to burn Li. As a consequence, Li is depleted at early ages for cool stars. The comparison of this Li abundance to that of

⁹PAdova and TRieste Stellar Evolutionary Code: <http://stev.oapd.inaf.it/cgi-bin/cmd>

¹⁰ $A(\text{Li}) = \log[N(\text{Li})/N(\text{H})] + 12$

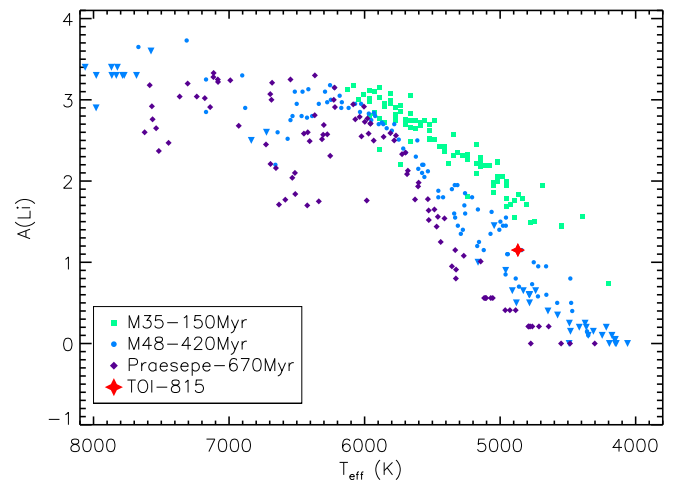


Fig. 5: Lithium abundance as a function of T_{eff} . The green, blue and purple points represent the position of targets in M35 (Sestito & Randich 2005; Anthony-Twarog et al. 2018), M48 (Sun et al. 2023), and Praesepe (Cummings et al. 2017) clusters, respectively. TOI-815 is marked in red.

stars of similar T_{eff} in open clusters also points to a very young age. In particular, the stars around 4900 K in the Hyades (with an age of ~ 600 Myr) have $A(\text{Li})$ below 1 dex (see Fig. 5 in Sestito & Randich 2005). Similar values are observed in Praesepe, with an age of ~ 670 Myr (Cummings et al. 2017). Therefore, TOI-815 should be younger than the Hyades and Praesepe. On the other hand, for clusters of 150-250 Myr (e.g. M35, NGC 6475, M34) analysed in (Sestito & Randich 2005; Anthony-Twarog et al. 2018), stars with $T_{\text{eff}} \sim 4900$ K have Li around 1.5 dex. The recent work on M48, a 420 Myr old cluster (Sun et al. 2023) shows that stars with effective temperatures near 4900 K have lower Li values (around 1 dex) than TOI-815, adding an additional constraint for an age younger than ~ 400 Myr. The Li abundance of TOI-815 is shown with those clusters as comparison in Figure 5.

To gain a more precise understanding of TOI-815's age we utilise a recently developed kinematic-based method (Maciel et al. 2011; Almeida-Fernandes & Rocha-Pinto 2018) that relies on a higher probability of kinematic disturbances and thus stellar Galactic velocity relative to known kinematic families over the lifetimes of stars (Wielen 1977; Nordström et al. 2004; Casagrande et al. 2011). We compared the Galactic U , V , and W velocities of TOI-815 to kinematic-age probability distributions bench-marked using a sample of 9000 stars with well-known isochronal ages Almeida-Fernandes & Rocha-Pinto (2018) and determine a nominal age of ~ 470 Myr.

Finally, the gyrochronological relations of Barnes (2007) and the rotation period of $P_{\text{rot}} = 15.3 \pm 1.2$ days constrained from the photometry (Section 3.3) suggest an age of 660 ± 150 Myr.

3.3. Stellar rotation

Using the ESPRESSO RVs, we measured a median $\log R'_{\text{HK}} = -4.67 \pm 0.03$, which suggests that TOI-815 is a quite active (see Fig. 7 in Henry et al. 1996) star. Visual inspection of the raw TESS transit light curves shows a sinusoidal variation which is likely attributed to the stellar activity (Figure A.1). For our analysis, we used the generalized Lomb-Scargle (GLS; Zechmeister & Kürster 2009) on the TESS SAP photometry of Sector 63 and we identified a significant periodic signal with a period of ~ 16.5

days, which could be associated to the stellar rotation (Figure D.1). TOI-815 was also observed by the WASP transit survey (Pollacco et al. 2006) in multiple years between 2006 and 2014, with the observing season in each year spanning ~ 120 nights. A total of 86 000 photometric data points was obtained using 200-mm, f/1.8 Canon lenses until 2012 and 85-mm f/1.2 Canon lenses after that. TOI-815 is by far the brightest star in the extraction aperture. In the years 2008, 2012 & 2013 we detect a significant periodicity with a period of 14.2–15.7 days. In each of those years the estimated FAP is below 1%. By combining the TESS Sector 63 and WASP photometric data, we estimate the stellar rotation to be 15.3 ± 1.2 days.

We repeated the frequency analysis for the ESPRESSO RV measurements, as well as for the Ca II H&K activity index ($\log R'_{HK}$) and the CCF asymmetry indicators (FWHM and bisector). The GLS periodogram of the RV measurements shows a strong peak at the orbital frequency of TOI-815c ($P_{\text{orb,c}} \sim 35$ days) with a FAP $< 1\%$. Following the subtraction of the outer planet's signal, we found a significant peak at the orbital period of TOI-815b ($P_{\text{orb,b}} \sim 11.2$ days) with a FAP $\approx 1\%$. Moreover, the stellar rotation period has no counterpart in the GLS periodograms of the RVs or the activity indicators.

The most straightforward way to estimate the stellar inclination is to assume solid body rotation (e.g. Borucki & Summers 1984; Doyle et al. 1984)

$$\sin i_{\star} = \frac{v \sin i_{\star}}{v} = \frac{v \sin i_{\star}}{2\pi R_{\star}/P_{\text{rot}}}, \quad (1)$$

where P_{rot} is the stellar equatorial rotation period. However, directly using Eq. (1) to generate an i_{\star} distribution is hazardous, because $v \sin i_{\star}$ and P_{rot} are correlated quantities (Masuda & Winn 2020). So as to avoid such interdependency biases, we use the same procedure as Attia et al. (2023) to derive the stellar inclination. We fit for $v \sin i_{\star}$ with a Markov chain Monte Carlo (MCMC, using the emcee package, Foreman-Mackey et al. 2013) based on the following formulation of Eq. (1)

$$v \sin i_{\star} = \frac{2\pi R_{\star}}{P_{\text{rot}}} \sqrt{1 - \cos^2 i_{\star}}, \quad (2)$$

and using a semi-Gaussian distribution for $v \sin i_{\star}$ (since we only have an upper limit) as a constraint for the computation of the likelihood. We set R_{\star} , P_{rot} , and $\cos i_{\star}$ as independent jump parameters with measurement-informed Gaussian priors on R_{\star} and P_{rot} (Table 1), and a uniform prior on $\cos i_{\star}$ (i.e. assuming an isotropic stellar inclination distribution). The number of walkers and the burn-in phase are adjusted to ensure the convergence of the chains. The ensuing probability distribution function (PDF) yields $i_{\star} = 32^{+15}_{-23} \text{ }^{\circ}$, the posterior estimate corresponding to the median value and the error bars to the 68% highest density interval (HDI). This result indicates that the star is spinning faster ($v = 2.5 \pm 0.2 \text{ km s}^{-1}$) but we are observing it close to pole-on.

Additionally, we used the TESS photometric data to constrain the fraction of stellar surface covered with spots. For this, we used the SAGE¹¹ tool to obtain flux variability models for a given spot configuration. We fitted the observed variability using the same procedure as described in Chakraborty et al. (2023), with uniform priors on latitude, longitude and size of active regions. The wide priors allow spots to be present over the entire stellar surface and the spot sizes vary from small sun-like spots (1°) to large M-dwarf-type spots (15°). To limit the degeneracy

Table 1: Stellar parameters for TOI-815.

	TOI-815	Source
Identifiers		
TIC ID	102840239	TICv8
2MASS ID	J10232924-4350059	2MASS
Gaia ID	5415648821879172096	Gaia DR3
TYC	7721-01451-1	Tycho-2
Astrometric parameters		
Right ascension (J2016), α	$10^{\text{h}} 23^{\text{m}} 29.25^{\text{s}}$	Gaia DR3
Declination (J2016), δ	$-43^{\circ} 50' 05.84''$	Gaia DR3
Parallax (mas)	16.825 ± 0.013	Gaia DR3
Distance (pc)	59.437 ± 0.045	Gaia DR3
$\mu_{\text{RA.}}$ (mas yr $^{-1}$)	8.898 ± 0.011	Gaia DR3
μ_{Dec} (mas yr $^{-1}$)	7.248 ± 0.013	Gaia DR3
Photometric parameters		
TESS (mag)	9.360 ± 0.006	TICv8
B (mag)	11.145 ± 0.061	Tycho-2
V (mag)	10.217 ± 0.005	Tycho-2
G (mag)	9.9398 ± 0.0004	Gaia DR3
J (mag)	8.531 ± 0.024	2MASS
H (mag)	8.066 ± 0.029	2MASS
K (mag)	7.999 ± 0.029	2MASS
Bulk parameters		
Spectral type	K3	Sec. 3.1
T_{eff} (K)	4869 ± 77	Sec. 3.1
R_{\star} (R_{\odot})	0.770 ± 0.009	Sec. 3.2
M_{\star} (M_{\odot})	0.776 ± 0.036	Sec. 3.2
[Fe/H] (dex)	-0.09 ± 0.05	Sec. 3.1
[Si/H] (dex)	-0.03 ± 0.06	Sec. 3.1
[Mg/H] (dex)	-0.03 ± 0.09	Sec. 3.1
$\log g_{\star}$ (cm s $^{-2}$)	4.51 ± 0.04	Sec. 3.1
$v \sin i_{\star}$ (km s $^{-1}$)	< 1	Sec. 3.1
P_{rot} (days)	15.3 ± 1.2	Sec. 3.3
i_{\star} ($^{\circ}$)	32^{+15}_{-23}	Sec. 3.3
Age (Myr)	200^{+400}_{-200}	Sec. 3.2
A (Li) (dex)	1.15 ± 0.05	Sec. 3.2

Sources: 1) TICv8 (Stassun et al. 2019) 2) 2MASS (Skrutskie et al. 2006) 3) Gaia DR3 (Gaia Collaboration et al. 2021) 4) Tycho-2 (Høg et al. 2000).

on constraining the parameters of active regions, we fixed the stellar inclination (to 32°) and spot contrast in the TESS bandpass (to 0.2691). We iteratively increased the number of spots from 0 to 4 and found that a 1-spot model is most probable and has the lowest Bayesian Information Criterion (BIC). We conclude that at least $0.26^{+0.20}_{-0.05} \text{ %}$ of the stellar surface is covered with spots to match the observed photometric variability. We also estimated the impact of these variations on the radius determination of the planets to be below 0.31%.

4. Photometric and RV analysis

4.1. TESS only modelling

As mentioned in Section 2.2, visual inspection of the light curves of TOI-815 in Sector 9 and Sector 36 revealed two similar single transits incompatible with the known $P = 11.2$ days inner planet. The two transits were separated by a gap of 734.5 days which initially led to 41 separate period aliases between 17.49 days (P_{min}) and 734.5 days (P_{max}), where period on aliases shorter than this

¹¹<https://github.com/chakrah/sage>

Table 2: Fitted and derived parameters for TOI-815b and TOI-815c.

Parameter	TOI-815b	TOI-815c
Orbital period, P_{orb} (days)	$11.197259^{+0.000018}_{-0.000017}$	$34.976145^{+0.000099}_{-0.000097}$
Planet radius, R_p (R_{\oplus})	$2.94^{+0.05}_{-0.05}$	$2.62^{+0.10}_{-0.09}$
Planet mass, M_p (M_{\oplus})	$7.6^{+1.5}_{-1.4}$	$23.5^{+2.4}_{-2.4}$
Planet density, ρ_p (g cm^{-3})	$1.64^{+0.33}_{-0.31}$	$7.2^{+1.1}_{-1.0}$
Orbital inclination, i (degrees)	$89.36^{+0.17}_{-0.14}$	$89.107^{+0.026}_{-0.026}$
Impact parameter, b	$0.279^{+0.058}_{-0.073}$	$0.839^{+0.015}_{-0.016}$
Semi-major axis, a (au)	$0.0903^{+0.0018}_{-0.0019}$	$0.193^{+0.004}_{-0.004}$
Transit duration, T_{14} (hours)	$3.379^{+0.023}_{-0.023}$	$2.97^{+0.09}_{-0.10}$
Scaled semi-major axis, a/R_*	$25.2^{+0.6}_{-0.6}$	$53.9^{+1.3}_{-1.3}$
Equilibrium temperature ^(a) , T_{eq} (K)	686^{+13}_{-14}	469^{+9}_{-9}
Atmospheric scale height ^(b) , H (km)	288^{+58}_{-54}	51^{+7}_{-6}
Insolation ^(c) , S_p (S_{\oplus})	$36.9^{+2.9}_{-2.9}$	$8.03^{+0.64}_{-0.64}$
Restricted Jeans escape param. ^(d) , Λ	$28.6^{+5.7}_{-5.3}$	145^{+16}_{-16}

Notes: ^(a) The equilibrium temperature is calculated using $T_{\text{eq}} = T_{\text{eff}}(1 - A)^{1/4} \sqrt{\frac{R_*}{2a}}$, assuming a Bond albedo of $A = 0$. ^(b) The scale height is calculated using $H = \frac{k_B T_{\text{eq}}}{\mu g}$ assuming a mean molecular weight of 2.3 g/mol. ^(c) Insolation is calculated using $S_p = \frac{L_*}{4\pi a^2}$. ^(d) The restricted Jeans escape parameter is calculated using $\Lambda = \frac{GM_p m_H}{k_B T_{\text{eq}} R_p}$ (Fossati et al. 2017).

value would have produced a detectable third transit in TESS photometry. In order to determine the most likely periods, we modelled the system using `Monotools`¹² (Osborn 2022). This uses a period-agnostic fit of the two transit events, combined with priors from period, eccentricity and system stability to determine a marginalised posterior probability for each period. In the case of TOI-815c, we found that the inner-most aliases are most likely, with the 23 periods shorter than $P = 40$ days having probabilities greater than 1% (see Figure 6).

4.2. CHEOPS only modelling

We initially scheduled 13 of the most-likely period aliases of TOI-815c (all $P < 25$ days) with CHEOPS at varying priorities. This resulted in five observations in 2022, light curves for which are noted in Table F.1 and can be seen in Figure F.1. The most important observation occurred on 2022 March 17 (visit 3) which, due to its position exactly 367.25 days after the last transit (i.e. $t_1 + P_{\text{max}}/2$) was able to rule out half of all aliases. The CHESS program (PR110048) also observed a single observation of TOI-815b which showed little to no measurable transit timing variations (TTVs). Observations resumed in 2023, with a further seven aliases scheduled, of which five were observed. One such observation, on 2023 February 28 (visit 10), was serendipitously during the transit of planet b, adding a second CHEOPS transit. On 2023 March 19, TESS re-observed a third transit of TOI-815c. However, this occurred exactly 734.5 days after the previously observed transit (i.e. $t_2 = t_1 + P_{\text{max}}$), therefore no period information was gained from the observation of this transit. We extracted a quick-look lightcurve using TICA (Fausnaugh et al. 2020) in order to verify the position of this third transit and updated the ephemeris of scheduled aliases. Thanks to these observations, very few aliases with $P < 40$ days remained at this

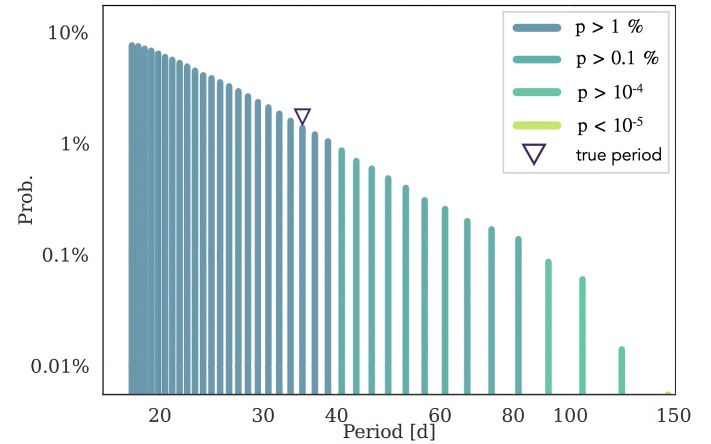


Fig. 6: Marginalised probabilities for each of the period aliases of TOI-815c as calculated by `Monotools`, from TESS data only. The triangle indicates the true period of the planet.

point. On 2023 April 23 (visit 11), a transit of TOI-815c at a unique transit time for the 34.97 days alias was finally observed with CHEOPS. Once a transit had been found all other observations were stopped. The CHEOPS light curves of TOI-815b and c are presented in Figure 7.

4.3. ESPRESSO only modelling

As discussed in Section 2.5, we conducted a spectroscopic follow-up of TOI-815 using ESPRESSO over a period of twenty months. In Figure D.1 we show that based on these observations we detected TOI-815c with a statistically significant signal at 35 days (FAP < 1%) and marginally detected TOI-815b at 11.2 days (FAP \sim 1%). After fixing the transit ephemerides, the signal of TOI-815c and b was detected at a 10σ and 5σ level, respectively.

4.4. Joint analysis

We performed an analysis of the planetary system around TOI-815 by combining photometric and RV data. To jointly model the datasets, we used the `juliet` software package which is a Bayesian framework capable of modeling multi-planet systems. `Juliet` is an openly accessible tool that enables simultaneous fitting of both transit models (using the `batman` package, Kreidberg 2015) and radial velocities (RVs) (via the `radvel` package, Fulton et al. 2018). It incorporates GPs to model noise (via the `celerite` package, Foreman-Mackey et al. 2017). To explore the parameter space, the code uses nested sampling algorithms with `dynesty` (Speagle 2020) and conducts model comparison through Bayesian evidences (lnZ) using `MultiNest` (Feroz et al. 2009) in conjunction with the `PyMultiNest` (Buchner et al. 2014) Python software package.

`Juliet` employs an efficient parametrization technique for the transit model by fitting the parameters r_1 and r_2 , which are a combination of the planet-to-star ratio (p) and impact parameter (b). This approach ensures a uniform exploration of the (p, b) space. Furthermore, `Juliet` estimates the stellar density ρ_* , which, when combined with the orbital period, determines the scaled semi-major axis (a/R_*).

To account for TESS photometric variability, we included a GP for Sector 36 and 63 using a `celerite` (approximate) Matérn-

¹²<https://github.com/hposborn/MonoTools>

3/2 kernel with hyperparameters amplitude (σ_{GP}) and timescale (ρ_{GP}) as shown in Figure A.1. The CHEOPS light curves exhibit correlations with certain instrumental parameters like contamination by background stars (bg), centroid movements (x, y) and the change in temperature of the telescope tube ΔT . Additionally, periodic noise features occur once per CHEOPS orbit due to the satellite's rolling motion around its pointing direction. To account for these periodic instrumental effects, we detrended the light curves by considering the sine or cosine of the roll angle (ϕ). In our global analysis, we incorporated linear models to account for both instrumental trends and stellar variability. However, it was essential to select only the relevant detrending parameters for each specific CHEOPS observation. To achieve this, we employed the `pycheops` package (Maxted et al. 2022) that provided us with the optimal combination of detrending terms for each visit. The detrending terms for each CHEOPS visit are listed in Table F.1.

The stellar density was fitted using a Gaussian prior based on the stellar spectroscopic analysis conducted in Section 3. We derived the quadratic stellar limb-darkening coefficients and their uncertainties for each photometric filter used using the LDCU¹⁴ code (Deline et al. 2022). The LDCU code computes the limb-darkening coefficients and their corresponding uncertainties by considering a set of stellar intensity profiles and accounting for the uncertainties on the stellar parameters. In our global analysis, we utilized the determined limb-darkening coefficients from LDCU as Gaussian priors for all TESS, CHEOPS, LCOGT and ASTEP data.

The SPOC crowding metric calculated for TOI-815 in Sector 36 and 63 is ~ 0.85 . This indicates that, according to SPOC modeling after eliminating background noise, $\sim 85\%$ of the flux detected within the photometric aperture originated from the target star. The remaining 15% was attributed to various other sources, with source 2 (TIC 102840237; Section 2.1) being particularly significant. To compensate for contamination by these additional sources, we fixed the dilution factor for all the light curves to 0.85.

In order to prevent any potential Lucy-Sweeney bias in the eccentricity measurement (Lucy & Sweeney 1971), we fixed the orbital eccentricity to zero. However, to explore the possibility of non-circular orbits, we run a separate analysis without any constraints on the eccentricity. With the eccentricity fitted, we found a value of $e = 0.110^{+0.072}_{-0.065}$ for TOI-815b and $0.035^{+0.064}_{-0.016}$ for TOI-815c. Therefore, the condition $e > 2.45\sigma_e$ is not satisfied, which suggests that the RV data are compatible with a circular orbit. Additionally, in Table E.1 we show that the 3σ upper limit on the eccentricity for TOI-815b and TOI-815c is 0.20 and 0.22, respectively.

5. Discussion

We report the discovery and characterization of two transiting mini-Neptune planets around TOI-815, a young K3V star. TOI-815b is a 11.2 days period planet with a radius of $2.94 \pm 0.05 R_{\oplus}$ and a mass of $7.6 \pm 1.5 M_{\oplus}$. The outermost planet, TOI-815c, has an orbital period of 35 days, a radius of $2.62 \pm 0.10 R_{\oplus}$ and a mass of $23.5 \pm 2.4 M_{\oplus}$. Based on the stellar parameters (Table 1), we find that the semimajor axis of TOI-815b and TOI-815c are 0.0903 ± 0.0019 au and 0.193 ± 0.004 au, respectively. Assuming a zero albedo and full heat redistribution ($f = 1$), the equilibrium temperature of the inner planet is 686^{+13}_{-14} K and its

stellar insolation is $36.9 \pm 2.9 S_{\oplus}$. The outer planet has an equilibrium temperature of 469^{+9}_{-9} K and receives a total amount of insolation equal to $8.03 \pm 0.64 S_{\oplus}$.

Both planets lie within the population of sub-Neptunes that are transiting FGK stars, with 87 well-characterized exoplanet detections¹ (including TOI-815b and TOI-815c) from the PlanetS catalog². TESS has contributed in this sample with 46 discoveries during the past five years (Naponiello et al. 2023). Moreover, TOI-815c adds to the population of warm mini-Neptune-sized planets with low stellar irradiation (less than $30 S_{\oplus}$) comprising a total of 21 well-characterized detections. Figure 8 places TOI-815b and TOI-815c in the mass-radius diagram of small exoplanets ($2-4 R_{\oplus}$) with precise densities orbiting FGK stars (gray points). The red triangles correspond to exoplanets with stellar irradiation lower than $30 S_{\oplus}$. The composition lines of pure-silicates (Zeng et al. 2016), Earth-like planets, and pure-iron (Dorn et al. 2015) are displayed in gray, light-brown, and brown, respectively. We also plot two other composition lines from Aguichine et al. (2021) as dashed and dotted black lines. For TOI-815b, we plot a line at 700 K, corresponding to its equilibrium temperature, with a composition of 45% of water and the rest as an Earth-like composition (32.5% iron-67.5% silicates). Since TOI-815c is denser and less irradiated, we can see that it lies on the composition lines with 10% water and an Earth-like composition at 450 K, its equilibrium temperature. Finally, we can say that if TOI-815b is rich in water for the model under consideration, its atmosphere is inflated by its irradiation, giving it a large radius and therefore a low density for a quantity of water of around 45%. TOI-815c, on the other hand, would have a lower water content of less than 10%, and its lower irradiation would not have as much influence as its neighbor on its radius, which would explain its higher density. Of course, this remains one possible model, and it is worth remembering that the position of a planet in the mass-radius diagram does not uniquely determine its composition. These planets could also have atmospheres rich in H/He or heavier materials. A more detailed discussion of the internal structures can be found in Section 5.3.

5.1. Density discrepancy of low and highly irradiated mini-Neptunes

TOI-815c with a bulk density of $7.2 \pm 1.1 \text{ g cm}^{-3}$ becomes the densest, well-characterized, warm mini-Neptune ($2-4 R_{\oplus}$ and $\leq 30 S_{\oplus}$) with GJ 143b ($\rho_p = 7.0 \pm 1.6 \text{ g cm}^{-3}$ and $S_p = 6.0 \pm 0.4 S_{\oplus}$; Dragomir et al. 2019) being the second one. Also, TOI-815c is the third densest, well-characterized mini-Neptune ($2-4 R_{\oplus}$) with the other two being K2-292b ($\rho_p = 7.4 \pm 1.6 \text{ g cm}^{-3}$ and $S_p = 72 \pm 11 S_{\oplus}$; Luque et al. 2019) and Kepler-411b ($\rho_p = 10.3 \pm 1.3 \text{ g cm}^{-3}$ and $S_p = 196 \pm 9 S_{\oplus}$; Sun et al. 2019). We analyse the differences in bulk density of planets with $2-4 R_{\oplus}$ and $\leq 30 S_{\oplus}$ ("warm" sub-Neptunes) and planets of the same size but with $\geq 30 S_{\oplus}$ ("hot" sub-Neptunes). In the first group, we have 21 planets with a median density of 3.9 g cm^{-3} . In the second, we have 65 planets with a median density of 2.9 g cm^{-3} . We perform a resampling method, to account for uncertainties in density measurements: a large number of new data sets ($N = 10,000$ samples) are drawn, which lie within the normal distribution of the density measurements of the planets. For each of these new data sets, the Kernel Density Estimation (KDE) is calculated. Similar to histograms, its aim is to estimate an unknown probability density function from a sample of data but in a more continuous way. We then calculate the mean and standard deviation of all the KDEs obtained. The result for the two groups is shown in Figure 9. There is evidence suggesting that sub-Neptune-size

¹⁴<https://github.com/delinea/LDCU>

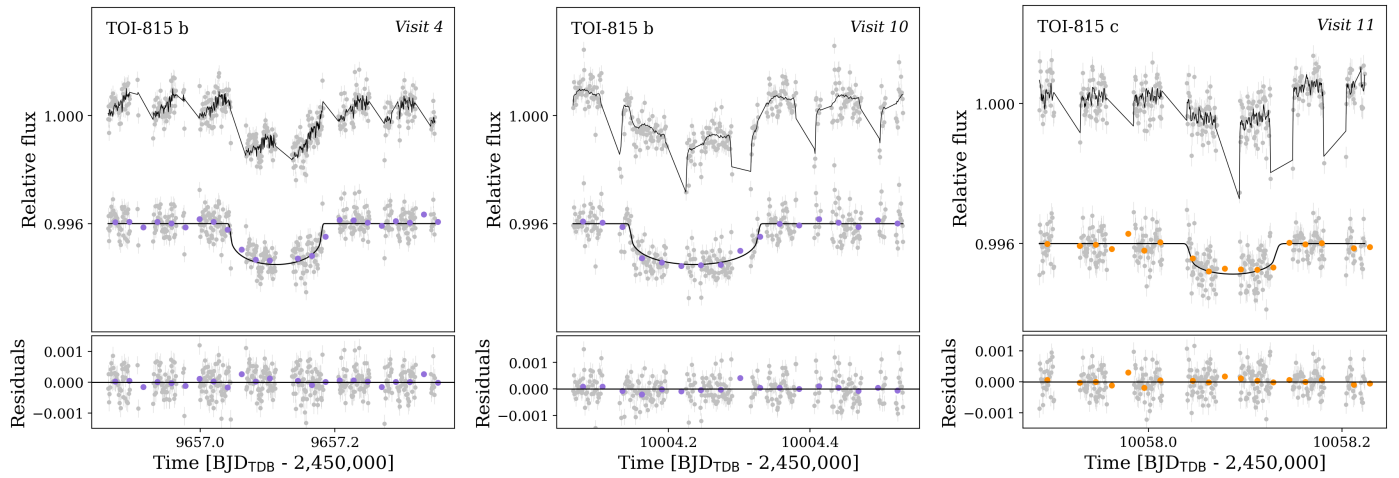


Fig. 7: CHEOPS light curves of TOI-815b (visit 4 and 10) and TOI-815c (visit 11). The top light curves in the upper panel present the raw flux and the best-fit decorrelation model. The detrending terms are presented in Table F.1. The bottom light curves in the upper panel present the detrended flux with the best-fit transit model overlaid in black. The residuals of the models are shown in the lower panel. The data are binned to 30 minutes (purple and orange circles).

planets orbiting FGK stars with low stellar irradiation ("warm" sub-Neptunes) exhibit a slightly higher bulk density compared to those exposed to strong irradiation. To test whether the difference in densities of planets in these two irradiation conditions is statistically significant, we utilize a two-sample Kolmogorov-Smirnov (K-S) test, which studies whether the two data samples come from the same distribution. With a p-value of 0.026, we find that the densities of hot and warm sub-Neptunes belong to different distributions with over 95% confidence. The inclusion of TOI-815b and c in the samples plays an important role in the statistical significance of this result, as they reduce the p-value from 0.051 to 0.026, enabling us to reach the 95% confidence interval. This difference in density could potentially be attributed to the cooler atmospheres of these less irradiated planets, which are more compressed and denser. However, such pattern could be also linked to observational bias since more massive planets at long periods are easier to characterize using RVs. Therefore, further precise measurements of the mass of similar exoplanets using precise radial velocities are necessary.

5.2. Similarity in density of multi-planet systems

Well-characterized exoplanets in multi-planet systems are especially interesting since they allow for investigation of the system's architecture. Otegi et al. (2022) studied the similarity of planets in radii, masses, densities, and period ratios within a multi-planet system and revealed that planets tend to be more similar in radius than in mass. This trend could be linked to the significant influence of the planetary radius on density compared to mass, and consequently, on the overall planetary composition. Interestingly, in their work, they observed a robust correlation between densities of adjacent planets with no clear evidence of bi-modality.

In our study we used the NASA Exoplanet Archive¹⁶ (Akeson et al. 2013) and narrowed down our selection to planets exhibiting mass and radius uncertainties below $\sigma_M/M \leq 50\%$ and $\sigma_R/R \leq 16\%$. For planets with masses characterized by TTVs we used the catalogue presented by Hadden & Lithwick (2017) and discarded the less robust (Kepler-25b and c, Marcy et al. 2014;

Kepler-18c, Cochran et al. 2011). Our final sample consists of 116 planets within 39 multi-planet systems. In Figure 10 we plot the density of a planet (j) within our sample against the density of the next planet ($j+1$) farther from the star. The points are color-coded by the host effective temperature. The Pearson correlation test resulted in a p-value = 0.04 that suggests a statistically significant linear correlation between densities. It's worth noting that planets orbiting M-dwarf stars tend to be closer to the 1:1 line compared to FGK stars with a p-value = 0.03. However, it's important to bear in mind that this observation is based on a limited sample of 22 planets within 9 multi-planet systems. We calculated the similarity metric for the TOI-815 system using Eq. (2) in Millholland et al. (2017):

$$\mathcal{D}_X = \sum_{i=1}^{N_{\text{sys}}} \sum_{\substack{j=1 \\ P_j < P_{j+1}}}^{N_{\text{pl}}-1} \left| \log \frac{X_{j+1}}{X_j} \right|, \quad (3)$$

with X corresponding to the planetary radius or planetary mass, to be $\mathcal{D}_R = 0.05$ and $\mathcal{D}_M = 0.49$. The metrics indicate that the planets in the TOI-815 system are very similar in radii but rather different in mass. Placing the TOI-815 system in Figure 10, we clearly see that TOI-815 is one of the least uniform systems in density. Similar to TOI-815, the Kepler-107 system (Bonomo et al. 2023) consists of two planets, Kepler-107b and c, with nearly identical radii ($1.536 \pm 0.025 R_{\oplus}$ and $1.597 \pm 0.026 R_{\oplus}$) but significantly different densities ($5.8^{+2.7}_{-2.6} \text{ g cm}^{-3}$ and $13.5^{+2.9}_{-2.8} \text{ g cm}^{-3}$). Bonomo et al. (2019) showed that this density discrepancy can be explained by a giant impact on Kepler-107c. As presented in Section 5.4, such mechanism can explain the large density of TOI-815c which suggests that the two planets have formed in a similar way.

5.3. Planetary composition and internal structure

As shown in Figure 8, the TOI-815 planetary system consists of two exoplanets that are located above an Earth-like composition line in the M-R diagram. This already indicates that both planets include a considerable amount of volatile materials, and for TOI-815b, a sizable atmosphere.

¹⁶<https://exoplanetarchive.ipac.caltech.edu/>

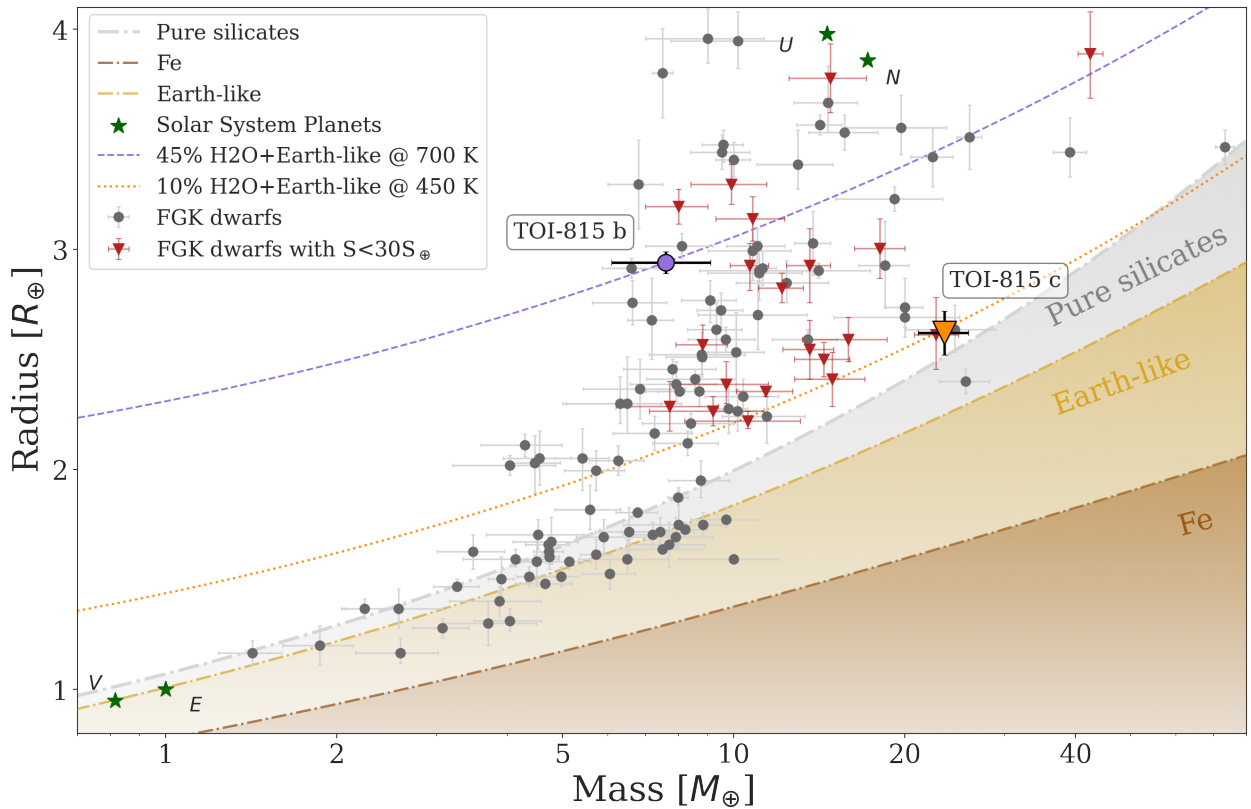


Fig. 8: The mass-radius diagram of small exoplanets (with radii ranging from 2 to 4 R_{\oplus}) with precise densities¹ from the PlanetS catalog² orbiting FGK stars. The red triangles correspond to exoplanets with stellar irradiation lower than $30 S_{\oplus}$. The composition lines of pure-silicates (gray) from Zeng et al. (2016), Earth-like planets (light-brown), and pure-iron (brown) from Dorn et al. (2015) are displayed. The purple and orange points represent TOI-815b and c, respectively. Two composition lines (Aguichine et al. 2021) that incorporate both water and terrestrial elements matching the equilibrium temperatures of the two planets are plotted as purple dashed and orange dotted lines.

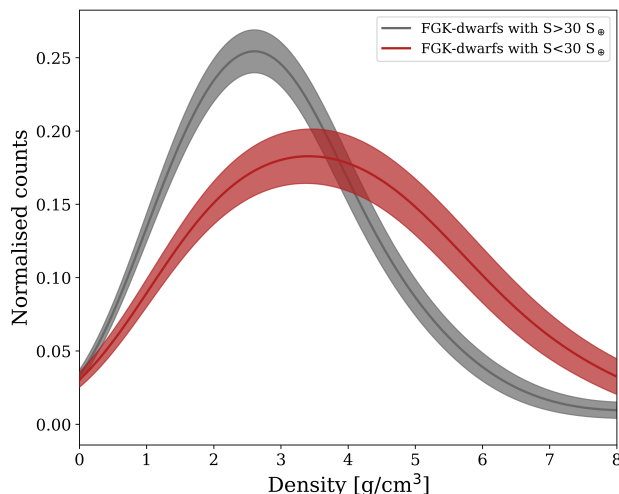


Fig. 9: Kernel Density Estimation (KDE) for the two groups of Sub-Neptunes (2-4 R_{\oplus}): with an irradiation above $30 S_{\oplus}$ (grey) and below $30 S_{\oplus}$ (red). The solid line represents the mean of the KDEs calculated with the 10, 000 samples drawn and the transparent region represents the standard deviation.

To explore the range of possible interior structures, we used a nested sampling algorithm (Buchner et al. 2014) on the four-

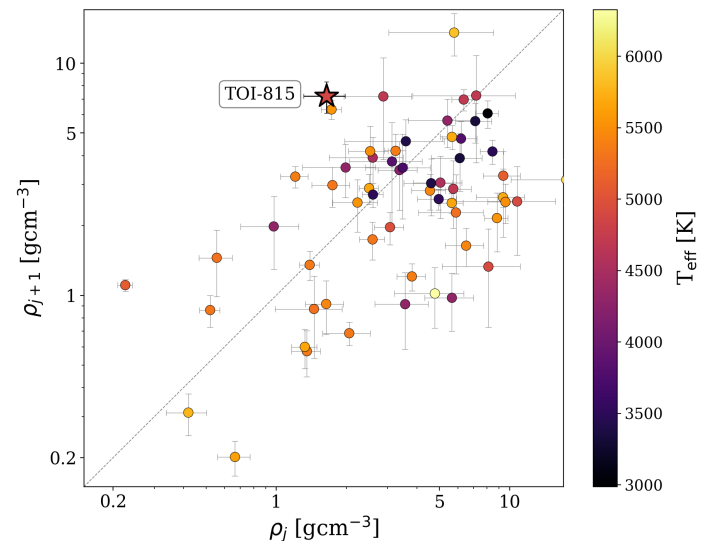


Fig. 10: The density of a planet (j) against the density of the next planet ($j+1$; farther from the star). The TOI-815 system is indicated with a star symbol.

layered interior model (Dorn et al. 2017). This model contains an iron core, a rocky mantle, a water layer, and a H-He atmosphere. For both planets, we ran two bracketing interior models: One

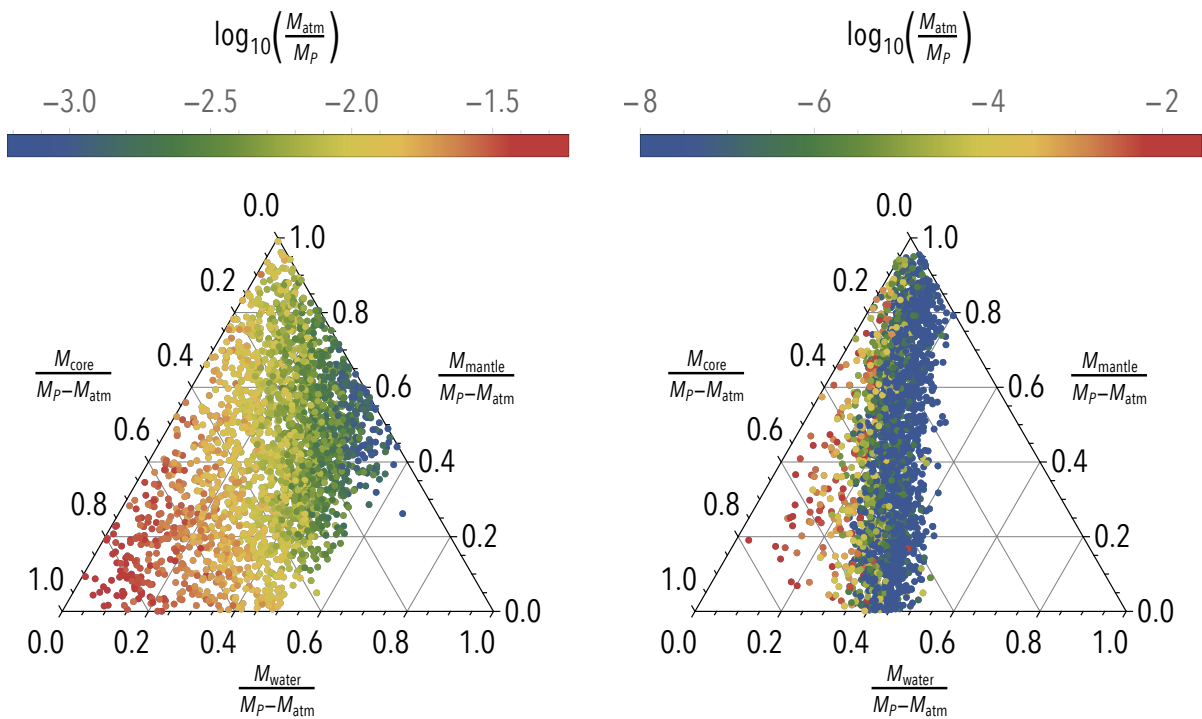


Fig. 11: Ternary plots of the nested sampling results for the *free model* of TOI-815b (left) and TOI-815c (right), respectively. The axes are normalized with respect to $M_p - M_{\text{atm}}$ and the color of the points indicate the atmospheric mass fraction in logarithmic scale.

where we put no constraints on the layer masses (*free model*), and one where we set the water mass fraction to zero in order to put an upper limit on the atmospheric mass fraction (*no-water model*). Additionally, for TOI-815c, we included a model where we set the atmospheric mass fraction to zero (*no-atmosphere model*). Such a model is not possible for TOI-815b, as its radius is too large to have no atmosphere. For all models, we vary the elemental ratios of [Fe/Si] and [Mg/Si] in the mantle and the planetary age, while we cap the water mass fraction at 50%. As a proxy for the planet's age, we use the age constraints of the host star. The results are summarized in Table 3 and Figure 11.

Table 3: Nested sampling results for the interior structure of the *free* model (top), the *no-water* model (middle), and the *no-atmosphere* model (bottom).

Planet (model)	M_{core}/M_p	M_{mantle}/M_p	M_{water}/M_p	$\log(M_{\text{atm}}/M_p)$
<i>free:</i>				
TOI-815b	0.29 ± 0.20	0.42 ± 0.22	0.28 ± 0.13	-2.16 ± 0.40
TOI-815c	0.32 ± 0.16	0.44 ± 0.26	0.23 ± 0.12	-7.70 ± 2.69
<i>no-water:</i>				
TOI-815b	0.40 ± 0.25	0.58 ± 0.26	0	-1.64 ± 0.22
TOI-815c	0.30 ± 0.23	0.70 ± 0.24	0	-2.78 ± 0.75
<i>no-atmosphere:</i>				
TOI-815c	0.31 ± 0.15	0.43 ± 0.25	0.26 ± 0.11	N/A

As expected, we find that a plethora of interior structures are consistent with the observational constraints of TOI-815b and TOI-815c. These range from water-rich structures with little to no atmosphere in the case of TOI-815c, to structures devoid of water but with a non-negligible H-He atmosphere. However, while the internal structure of TOI-815b is rather poorly constrained, it is clear that the observational constraints can only be satisfied with an H-He atmosphere. This is in alignment with

Hakim et al. (2018) who calculated the mass-radius diagram with different core and mantle compositions for planets with Moon-like, Earth-like, or Mercury-like internal structures. Even though they obtained a broad distribution of planetary radii for planets of the same mass, none of the models without an atmosphere can reproduce the large radius of TOI-815b. This further supports the conclusion that it is impossible to construct a model of TOI-815b without a H-He atmosphere.

We emphasize that our interior structure model does not include the pollution of the H-He envelope with heavier elements, which leads to contraction of the atmosphere (e.g., Lozovsky et al. 2018). Furthermore, water might not only be present in an ocean layer, but also dissolved within the mantle of the planet (e.g., Dorn & Lichtenberg 2021) or be present in the atmosphere (e.g., Mol Lous et al. 2022). In addition, the assumption of distinct planetary layers might break down at high planetary masses (Helled & Stevenson 2017; Bodenheimer et al. 2018). Nonetheless, in face of the observational constraints currently available, these additions are unlikely to affect the main conclusions of this analysis.

5.4. Planetary atmospheric evolution

To model the atmospheric evolution of the planets in the TOI-815 system and constrain their primordial parameters, we present modelling conducted using the Planetary Atmospheres and Stellar RoTation RAtes (PASTA; Bonfanti et al. 2021b) code, which is a planetary atmospheric evolution code based on the original code presented by Kubyshkina et al. (2019a,b). As stars can be born with different initial rotation periods, their L_{XUV} values can spread over a wide range during the first ~ 1 Gyr following protoplanetary disk dispersal (e.g. Tu et al. 2015). To account for that, PASTA simultaneously constrains the evolution of

planetary atmospheres and of the stellar rotation rate by combining a model predicting planetary atmospheric escape rates based on hydrodynamic simulations (this has the advantage over other commonly used analytical estimates in that it accounts for both XUV-driven and core-powered mass loss; [Kubyshina et al. 2018](#)), a model of the evolution of the stellar XUV flux ([Bonfanti et al. 2021b](#)), a model relating planetary parameters and atmospheric mass ([Johnstone et al. 2015b](#)), and stellar evolutionary tracks ([Choi et al. 2016](#)).

PASTA works under two main assumptions: (1) planet migration did not occur after the dispersal of the protoplanetary disk; and (2) the planets hosted at some point in the past or still host a hydrogen-dominated atmosphere. The free parameters (i.e. subject to uniform priors) are the planetary initial atmospheric mass fractions at the time of the dispersal of the protoplanetary disk ($f_{\text{atm}}^{\text{start}}$), which we assume occurs at an age of 5 Myr (see for example [Alexander et al. 2014](#); [Kimura et al. 2016](#); [Gorti et al. 2016](#)), and the stellar rotation period at 150 Myr, which is used as a proxy for the stellar XUV emission. The code returns constraints on the free parameters and on their uncertainties by implementing the atmospheric evolution algorithm in a Bayesian framework (through the MC3 code of [Cubillos et al. 2017](#)), using the system parameters with their uncertainties as input priors. Details of the algorithm can be found in [Bonfanti et al. \(2021b\)](#).

As a proxy for the evolution of the stellar rotation period, and thus XUV emission, Figure 12 displays the posterior distribution of the stellar rotation period at an age of 150 Myr ($P_{\text{rot},150}$). This distribution is then compared to that of stars member of young open clusters that are of comparable mass, as obtained from [Johnstone et al. \(2015a\)](#). Because the system is still very young (200^{+400}_{-200} Myr), the posterior distribution of $P_{\text{rot},150}$ is mostly dominated by the measurement of the present-day rotation rate (15.3 ± 1.2 days). The distribution is however flatter than the prior on P_{rot} , because of the large relative uncertainty of the stellar age. The result indicates that the star could not be a fast rotator (i.e. $P_{\text{rot},150} < 1$ days), as constrained by the slow present-day rotation period.

Figure 13 shows the posterior distribution of the initial atmospheric mass fraction for TOI-815b (left panel) and TOI-815c (right panel) in comparison to the present-day atmospheric mass fraction. For planet b we find that PASTA clearly prefers evolutionary scenarios in which the evolution of the atmosphere was mostly unaffected by hydrodynamic escape. This indicates that the planet most likely still retains the majority of its primordial atmosphere. However, it must be noted that given the uncertainties of the observed present-day parameters PASTA is not able to completely exclude scenarios with significant escape.

In the case of TOI-815c, PASTA concludes that independently of the evolution of the stellar rotation rate, the planet has not lost a significant amount of atmosphere via hydrodynamic escape. Given its present-day orbital position and relatively large core-mass, it would be expected for the planet to have accreted an extensive hydrogen atmosphere if it had formed within the protoplanetary disk ([Ikoma & Hori 2012](#); [Lee & Chiang 2015](#); [Mordasini 2020](#); [Venturini & Helled 2017](#)). However, such an envelope is not observed today and according to PASTA the planet is unable to have lost it due to hydrodynamic escape over the course of its evolution. One possible explanation would be formation within a gas-poor environment (e.g. [Lee et al. 2022](#)). Another explanation is that the planet suffered from at least one giant impact towards the end of the disc life ([Inamdar & Schlichting 2015](#)). This also aligns with the fact that the planets of the system are not in mean motion resonance and the expected spin-orbit misalignment. In both cases the results retrieved by PASTA

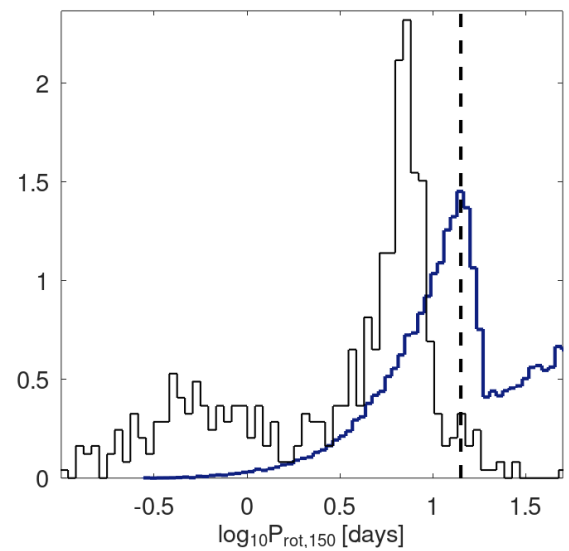


Fig. 12: Posterior distribution (dark blue) of the stellar rotation rate of TOI-815 after 150 Myr derived by PASTA. The solid black line represents the distribution of the stellar rotation rate of young open cluster stars with masses comparable to that of TOI-815 based on the collection of data provided by [Johnstone et al. \(2015a\)](#). The dashed black line indicates the observed present-day stellar rotation rate.

are compatible with conclusions that can be drawn by the more simplistic approach of only evaluating the Restricted Jeans Parameter Λ ([Fossati et al. 2017](#)). For TOI-815c the high value of $\Lambda = 145^{+16}_{-16}$ would imply a stable atmosphere, while for TOI-815b the intermediate value of $\Lambda = 28.6^{+5.7}_{-5.3}$ would favour a stable atmosphere but not exclude the possibility of a hydrodynamically escaping atmosphere. We note that in principle PASTA is not set up to simulate the atmospheric evolution of planets with mean planetary densities larger than that of Earth. This is due to the fact that the code always assumes for the rocky core of a planet to have a mean density equal to that of the Earth. In practice, PASTA will underestimate the planetary mass of TOI-815c as its observed density is $1.30 \pm 0.20 \rho_{\oplus}$. The planetary mass estimate for planet c returned by PASTA is $M_{\text{P,c}} = 19.9 \pm 1.9 M_{\oplus}$, which implies a bare rocky-core with a mean planetary density of $1 \rho_{\oplus}$. A larger planetary mass however would just further hinder hydrodynamic escape, as escaping particles would need even more energy to escape the gravitational well of the planet. Therefore, since hydrodynamic escape affects only marginally the evolution of the planetary atmosphere, the impact of the assumption on the core density has a negligible impact on the results.

5.5. Search for transit timing variations

Although the ratio of the orbital period of TOI-815 and c ($P_{\text{orb,c}}/P_{\text{orb,b}} \approx 3.12$) lies exterior to the 3:1 resonance, we conducted a TTV analysis to search for additional, non-transiting planets. Using `juliet`, we performed the analysis by utilizing all available photometric datasets from TESS, CHEOPS, ASTEP and LCOGT. Instead of fitting a single period (P_{orb}) and time-of-transit center (T_0), `juliet` employs a method that seeks individual transit times. This approach involves fitting each transit independently and determining one transit time for each one, resulting in a more consistent and coherent analysis. Figure 14 illustrates the results of our analysis, which compares the observed

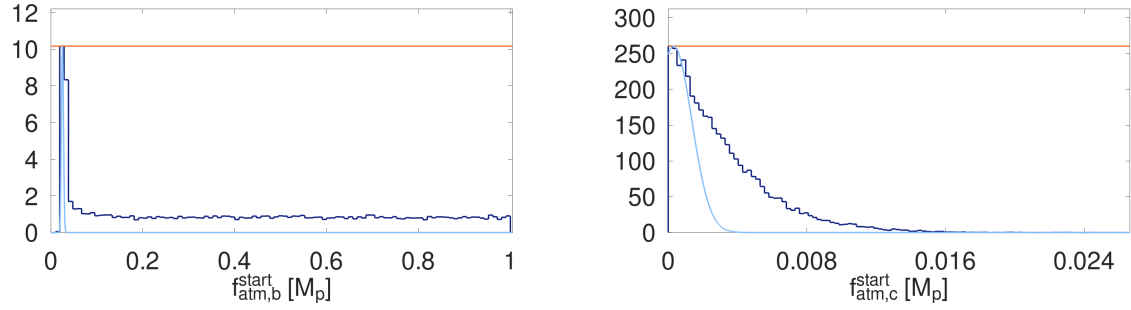


Fig. 13: Posterior distribution (dark blue) for the mass of the planetary atmosphere of TOI-815b (left) and TOI-815c (right) at the time of the dispersal of the protoplanetary disk. The light-blue line represents the distribution of the estimated present-day atmospheric mass fraction derived by PASTA. The orange horizontal line indicates the uninformative prior distribution.

transit times with the calculated linear ephemeris derived from all the transits. Notably, no significant variations were detected within the data.

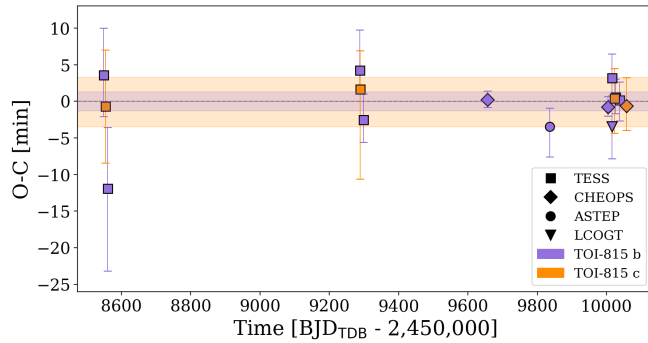


Fig. 14: Transit timings for each transit of TOI-815b (purple) and TOI-815c (orange) measured from the TESS and CHEOPS light curves. The purple and orange regions represent the 1σ uncertainties of the inner and outer planet ephemeris reported in Table E.1.

5.6. Potential for atmospheric and Rossiter-McLaughlin studies

We used the metric proposed by Kempton et al. (2018) to assess the potential of atmospheric characterization for the planets in the TOI-815 system with the James Webb Space Telescope (JWST, Gardner et al. 2023). To calculate the transmission spectroscopy metric (TSM) for all exoplanets in the PlanetS catalog² with a radii from 2 to $4 R_{\oplus}$, we utilized the scale factors provided in Table 1 by Kempton et al. (2018) instead of the suggested value of 0.167 for temperate planets. Notably, the TSM values for TOI-815b and c were found to be 97 ± 20 and 15 ± 2 , respectively. Putting these values into context, TOI-815b is located in the top 10% of well-characterized exoplanets in this regime and therefore stands out as an excellent candidate for atmospheric characterization via transmission spectroscopy.

We also explore the possibility of studying the spin-orbit of both planets via Rossiter-McLaughlin (RM) observations (Rossiter 1924; McLaughlin 1924). According to Eq. (40) by Winn (2010), we expect the maximum amplitude of the RM effect to be $\sim 1.13 \text{ m s}^{-1}$ and 0.52 m s^{-1} for TOI-815b and TOI-815c, respectively. Using the classical RM technique, the signals are small and challenging, but the sky-projected spin-orbit angle λ should be detectable using newer methods such as the

RM effect Revolutions (RMR) technique (Bourrier et al. 2021). Moreover, the star being seen close to pole-on and the planets being transiting, the two orbits are probably misaligned. This can be seen using the following equation linking the 3D spin-orbit angle ψ to other observable quantities (e.g., Winn et al. 2007):

$$\cos \psi = \sin i_{\star} \sin i \cos \lambda + \cos i_{\star} \cos i, \quad (4)$$

yielding a small value for $\cos \psi$ for any value of λ we measure. The case that would disfavor the orbital misalignment picture the most is if we observe an aligned sky-projected spin-orbit angle $\lambda \sim 0^\circ$. Sampling a ψ distribution from Eq. (4) with a Dirac distribution at 0° for λ and measurement-informed Gaussians for the other parameters, we find $\psi = 58^{+18}_{-19}$, which still represents a misaligned orbit at a 3.2σ level. Given the young nature of the system, tidal realignment (e.g., Barker & Ogilvie 2010; Attia et al. 2023) may have not had time to occur. Hence, TOI-815 offers us a unique possibility to capture a peculiar orbital architecture, especially given the scarcity of misaligned orbits in multi-planetary systems (e.g., Albrecht et al. 2022).

6. Conclusions

We have reported the detection and characterization of two sub-Neptune planets that are transiting TOI-815. TOI-815 is a young (200^{+400}_{-200} Myr) K-dwarf, in a K-M binary system. The planets were initially detected by the TESS mission and subsequently confirmed with CHEOPS observations as well as precise RV measurements obtained with ESPRESSO, which enabled the determination of their mass. Through the combined use of TESS, CHEOPS, LCOGT and ASTEP photometry and the ESPRESSO spectroscopic data, we precisely characterized both planets: TOI-815b has a period of 11.2 days, a radius of $2.94 R_{\oplus}$ and a mass of $7.6 M_{\oplus}$, while TOI-815c has a period of 35 days, a radius of $2.62 R_{\oplus}$ and a mass of $23.5 M_{\oplus}$. The combination of these facilities allowed us to determine the planetary radius and mass with precision better than 2% and 20% for the inner planet and 4% and 10% for the outer planet, respectively.

TOI-815c, with a bulk density of $7.2 \pm 1.1 \text{ g cm}^{-3}$, stands as the densest, well-characterized warm mini-Neptune. Our study reveals a statistically significant difference in bulk density between warm sub-Neptunes and hot sub-Neptunes, with TOI-815b and c being instrumental in establishing a 95% confidence. Further exoplanet detections with precise mass measurements are required in order to validate this trend. Our analysis of the TOI-815 system using similarity metrics demonstrated that while the planets in this system are remarkably similar in radii,

they exhibit significant differences in mass, making TOI-815 one of the least uniform systems in terms of planetary density.

Internal structure modeling including four layers (iron core, a rocky mantle, a water layer, and a H-He atmosphere) suggests that TOI-815b is likely to have a small H-He atmosphere (of the order of a percent) if water is included. If no water is assumed, the atmospheric mass fraction can be an order of magnitude higher. On the contrary, the radius of TOI-815c can be reproduced without any atmosphere. This object is interesting because it is rather massive, and yet seems to have only a tiny (or no) atmosphere. This is a challenge for planet formation theory since at these planetary masses strong accretion of H-He is expected (for comparison Uranus and Neptune have smaller masses but consist of $\sim 10\%$ of H-He). A possible explanation would be for the planet to have lost the majority of its primordial atmosphere. However, our atmospheric evolution model shows that such an extensive mass loss can not be caused by XUV-driven hydrodynamic escape. Thus, the most likely scenario is that planet c, similar to Kepler-107c (Bonomo et al. 2019), suffered from at least one giant impact (that removed substantial primordial gas) during the unstable dynamical phase of disc dispersal. This is consistent with the planets of this system not being in resonance. Alternatively, a formation within a gas-poor environment can also not be excluded.

Finally, the combination of the stellar rotation period ($P_{\text{rot}} = 15.3 \pm 1.2$ days) constrained from the WASP and TESS photometry and the very low spectroscopically measured projected rotational velocity ($v \sin i_* < 1 \text{ km s}^{-1}$) suggest that we are observing the star close to pole-on. Given the planets are on orbits with inclinations close to $\sim 90^\circ$, we expect a spin-orbit misalignment at a 3.2σ level. Future RM observations will be able to confirm this statement.

Acknowledgements. We thank the Swiss National Science Foundation (SNSF) and the Geneva University for their continuous support to our planet low-mass companion search programs. This work has been carried out within the framework of the National Centre of Competence in Research PlanetS supported by the Swiss National Science Foundation under grants 51NF40_182901 and 51NF40_205606. OA and VB have received funding from the European Research Council (ERC) under the European Union's Horizon 2020 research and innovation programme (project SPICE DUNE, grant agreement No 947634; grant agreement No 730890). This material reflects only the authors' views and the Commission is not liable for any use that may be made of the information contained therein. The authors acknowledge the financial support of the SNSF. This publication makes use of The Data & Analysis Center for Exoplanets (DACE), which is a facility based at the University of Geneva (CH) dedicated to extra-solar planet data visualization, exchange, and analysis. DACE is a platform of NCCR PlanetS and is available at <https://dace.unige.ch>. This paper includes data collected by the TESS mission. Funding for the TESS mission is provided by the NASA Explorer Program. JSJ acknowledges support by FONDECYT grant 1201371 and partial support from the ANID Basal project FB210003. Funding for the TESS mission is provided by NASA's Science Mission Directorate. KAC and CNW acknowledge support from the TESS mission via subaward s3449 from MIT. This research has made use of the Exoplanet Follow-up Observation Program (ExoFOP; DOI: 10.26134/ExoFOP5) website, which is operated by the California Institute of Technology, under contract with the National Aeronautics and Space Administration under the Exoplanet Exploration Program. This paper made use of data collected by the TESS mission and are publicly available from the Mikulski Archive for Space Telescopes (MAST) operated by the Space Telescope Science Institute (STScI). We acknowledge the use of public TESS data from pipelines at the TESS Science Office and at the TESS Science Processing Operations Center. Resources supporting this work were provided by the NASA High-End Computing (HEC) Program through the NASA Advanced Supercomputing (NAS) Division at Ames Research Center for the production of the SPOC data products. CHEOPS is an ESA mission in partnership with Switzerland with important contributions to the payload and the ground segment from Austria, Belgium, France, Germany, Hungary, Italy, Portugal, Spain, Sweden, and the United Kingdom. The CHEOPS Consortium would like to gratefully acknowledge the support received by all the agencies, offices, universities, and industries involved. Their flexibility and willingness to explore new approaches were essential to the success of this mission. CHEOPS data analysed in this article will be made available in the CHEOPS mission archive

(https://cheops.unige.ch/archive_browser/). This work makes use of observations from the ASTEP telescope. ASTEP benefited from the support of the French and Italian polar agencies IPEV and PNRA in the framework of the Concordia station program, from OCA, INSU, Idex UCAJEDI (ANR-15-IDEX-01) and ESA through the Science Faculty of the European Space Research and Technology Centre (ESTEC). This work makes use of observations from the LCOGT network. Part of the LCOGT telescope time was granted by NOIRLab through the Mid-Scale Innovations Program (MSIP). MSIP is funded by NSF Co-funded by the European Union (ERC, FIERCE, 101052347). Views and opinions expressed are however those of the author(s) only and do not necessarily reflect those of the European Union or the European Research Council. Neither the European Union nor the granting authority can be held responsible for them. C.B. acknowledges support from the Swiss Space Office through the ESA PRODEX program. This work has been carried out within the framework of the NCCR PlanetS supported by the Swiss National Science Foundation under grants 51NF40_182901 and 51NF40_205606. ML acknowledges support of the Swiss National Science Foundation under grant number PCEFP2_194576. S.G.S. acknowledge support from FCT through FCT contract nr. CEECIND/00826/2018 and POPH/FSE (EC). YAI acknowledges support from the Swiss National Science Foundation (SNSF) under grant 200020_192038. ABr was supported by the SNSA. DG gratefully acknowledges financial support from the CRT foundation under Grant No. 2018.2323 "Gaseous rocky? Unveiling the nature of small worlds". JV acknowledges support from the Swiss National Science Foundation (SNSF) under grant PZ00P2_208945. MNG is the ESA CHEOPS Project Scientist and Mission Representative, and as such also responsible for the Guest Observers (GO) Programme. MNG does not relay proprietary information between the GO and Guaranteed Time Observation (GTO) Programmes, and does not decide on the definition and target selection of the GTO Programme. KGI is the ESA CHEOPS Project Scientist and is responsible for the ESA CHEOPS Guest Observers Programme. She does not participate in, or contribute to, the definition of the Guaranteed Time Programme of the CHEOPS mission through which observations described in this paper have been taken, nor to any aspect of target selection for the programme. We acknowledge financial support from the Agencia Estatal de Investigación of the Ministerio de Ciencia e Innovación MCIN/AEI/10.13039/501100011033 and the ERDF "A way of making Europe" through projects PID2019-107061GB-C61, PID2019-107061GB-C66, PID2021-125627OB-C31, and PID2021-125627OB-C32, from the Centre of Excellence "Severo Ochoa" award to the Instituto de Astrofísica de Canarias (CEX2019-000920-S), from the Centre of Excellence "María de Maeztu" award to the Institut de Ciències de l'Espai (CEX2020-001058-M), and from the Generalitat de Catalunya/CERCA programme. S.C.C.B. acknowledges support from FCT through FCT contracts nr. IF/01312/2014/CP1215/CT0004. XB, SC, DG, MF and JL acknowledge their role as ESA-appointed CHEOPS science team members. LBo, GBr, VNa, IPa, GPi, RRa, GSc, VSi, and TZi acknowledge support from CHEOPS ASI-INAF agreement n. 2019-29-HH.0. ACC acknowledges support from STFC consolidated grant numbers ST/R000824/1 and ST/V000861/1, and UKSA grant number ST/R003203/1. P.E.C. is funded by the Austrian Science Fund (FWF) Erwin Schrödinger Fellowship, program J4595-N. This project was supported by the CNES. The Belgian participation to CHEOPS has been supported by the Belgian Federal Science Policy Office (BELSPO) in the framework of the PRODEX Program, and by the University of Liège through an ARC grant for Concerted Research Actions financed by the Wallonia-Brussels Federation; L.D. is an F.R.S.-FNRS Postdoctoral Researcher. This work was supported by FCT - Fundação para a Ciência e a Tecnologia through national funds and by FEDER through COMPETE2020 - Programa Operacional Competitividade e Internacionalização by these grants: UIDB/04434/2020; UIDP/04434/2020; 2022.06962.PTDC. O.D.S.D. is supported in the form of work contract (DL 57/2016/CP1364/CT0004) funded by national funds through FCT. S.G.S acknowledges the support from FCT through Investigador FCT contract nr. CEECIND/00826/2018 and POPH/FSE (EC). B.-O. D. acknowledges support from the Swiss State Secretariat for Education, Research and Innovation (SERI) under contract number MB22.00046. This project has received funding from the Swiss National Science Foundation for project 200021_200726. It has also been carried out within the framework of the National Centre of Competence in Research PlanetS supported by the Swiss National Science Foundation under grant 51NF40_205606. The authors acknowledge the financial support of the SNSF. MF and CMP gratefully acknowledge the support of the Swedish National Space Agency (DNR 65/19, 174/18). T.D. acknowledges support by the McDonnell Center for the Space Sciences at Washington University in St. Louis. M.G. is an F.R.S.-FNRS Senior Research Associate. CHe acknowledges support from the European Union H2020-MSCA-ITN-2019 under Grant Agreement no. 860470 (CHAMELEON). SH gratefully acknowledges CNES funding through the grant 837319. K.W.F.L. was supported by Deutsche Forschungsgemeinschaft grants RA714/14-1 within the DFG Schwerpunkt SPP 1992, Exploring the Diversity of Extrasolar Planets. This work was granted access to the HPC resources of MesoPSL financed by the Region Ile de France and the project Equip@Meso (reference ANR-10-EQPX-29-01) of the programme Investissements d'Avenir supervised by the Agence Nationale pour la Recherche. PM acknowledges support from STFC research grant num-

ber ST/M001040/1. This work was also partially supported by a grant from the Simons Foundation (PI Queloz, grant number 327127). A. S. acknowledges support from the Swiss Space Office through the ESA PRODEX program. TWi acknowledges support from the UKSA and the University of Warwick. NAW acknowledges UKSA grant ST/R004838/1. V.V.G. is an F.R.S.-FNRS Research Associate. C.D. acknowledges support from the Swiss National Science Foundation under grant TMSGI2_211313. GyMSz acknowledges the support of the Hungarian National Research, Development and Innovation Office (NKFIH) grant K-125015, a PRODEX Experiment Agreement No. 4000137122, the Lendület LP2018-7/2021 grant of the Hungarian Academy of Science and the support of the city of Szombathely. DR was supported by NASA under award number NNA16BD14C for NASA Academic Mission Services. R.L. acknowledges funding from University of La Laguna through the Margarita Salas Fellowship from the Spanish Ministry of Universities ref. UNI/551/2021-May 26, and under the EU Next Generation funds. R. A. is a Trottier Postdoctoral Fellow and acknowledges support from the Fonds de Recherche du Québec - Nature et Technologies (FRQNT). This work was funded by the Institut Trottier de Recherche sur les Exoplanètes (iREx). This work made use of `tpfpplotter` by J. Lillo-Box (publicly available in www.github.com/jlillo/tpfpplotter), which also made use of the python packages `astropy`, `lightkurve`, `matplotlib` and `numpy`.

References

Abe, L., Gonçalves, I., Agabi, A., et al. 2013, *A&A*, 553, A49

Adibekyan, V., Figueira, P., Santos, N. C., et al. 2015, *A&A*, 583, A94

Adibekyan, V. Z., Sousa, S. G., Santos, N. C., et al. 2012, *A&A*, 545, A32

Aguichine, A., Mousis, O., Deleuil, M., & Marcq, E. 2021, *ApJ*, 914, 84

Akeson, R. L., Chen, X., Ciardi, D., et al. 2013, *PASP*, 125, 989

Albrecht, S. H., Dawson, R. I., & Winn, J. N. 2022, *PASP*, 134, 082001

Alexander, R., Pascucci, I., Andrews, S., Armitage, P., & Cieza, L. 2014, in *Protostars and Planets VI*, ed. H. Beuther, R. S. Klessen, C. P. Dullemond, & T. Henning, 475–496

Aller, A., Lillo-Box, J., Jones, D., Miranda, L. F., & Barceló Forteza, S. 2020, *A&A*, 635, A128

Almeida-Fernandes, F. & Rocha-Pinto, H. J. 2018, *MNRAS*, 476, 184

Anthony-Twarog, B. J., Deliyannis, C. P., Harmer, D., et al. 2018, *AJ*, 156, 37

Attia, O., Bourrier, V., Delisles, J. B., & Eggenberger, P. 2023, *A&A*, 674, A120

Attia, O., Bourrier, V., Eggenberger, P., et al. 2021, *A&A*, 647, A40

Barker, A. J. & Ogilvie, G. I. 2010, *MNRAS*, 404, 1849

Barnes, S. A. 2007, *ApJ*, 669, 1167

Behmard, A., Dai, F., & Howard, A. W. 2022, *AJ*, 163, 160

Benz, W., Broeg, C., Fortier, A., et al. 2021, *Experimental Astronomy*, 51, 109

Berger, T. A., Huber, D., Gaidos, E., van Saders, J. L., & Weiss, L. M. 2020, *AJ*, 160, 108

Blackwell, D. E. & Shallis, M. J. 1977, *MNRAS*, 180, 177

Bodenheimer, P., Stevenson, D. J., Lissauer, J. J., & D'Angelo, G. 2018, *The Astrophysical Journal*, 868, 138

Bonfanti, A., Delrez, L., Hooton, M. J., et al. 2021a, *A&A*, 646, A157

Bonfanti, A., Fossati, L., Kubyshkina, D., & Cubillos, P. E. 2021b, *A&A*, 656, A157

Bonfanti, A., Ortolani, S., & Nascimbeni, V. 2016, *A&A*, 585, A5

Bonfanti, A., Ortolani, S., Piotto, G., & Nascimbeni, V. 2015, *A&A*, 575, A18

Bonomo, A. S., Dumusque, X., Massa, A., et al. 2023, *A&A*, 677, A33

Bonomo, A. S., Zeng, L., Damasso, M., et al. 2019, *Nature Astronomy*, 3, 416

Borucki, W. J. & Summers, A. L. 1984, *Icarus*, 58, 121

Bourrier, V., Lovis, C., Cretignier, M., et al. 2021, *A&A*, 654, A152

Brandeker, A., Heng, K., Lendl, M., et al. 2022, *A&A*, 659, L4

Brown, T. M., Baliber, N., Bianco, F. B., et al. 2013, *PASP*, 125, 1031

Buchner, J., Georgakakis, A., Nandra, K., et al. 2014, *A&A*, 564, A125

Casagrande, L., Schönrich, R., Asplund, M., et al. 2011, *A&A*, 530, A138

Castelli, F. & Kurucz, R. L. 2003, in *IAU Symposium*, Vol. 210, *Modelling of Stellar Atmospheres*, ed. N. Piskunov, W. W. Weiss, & D. F. Gray, A20

Chakraborty, H., Lendl, M., Akinsanmi, B., Petit dit de la Roche, D. J. M., & Deline, A. 2023, arXiv e-prints, arXiv:2311.16864

Choi, J., Dotter, A., Conroy, C., et al. 2016, *ApJ*, 823, 102

Cochran, W. D., Fabrycky, D. C., Torres, G., et al. 2011, *ApJS*, 197, 7

Collins, K. 2019, in *American Astronomical Society Meeting Abstracts*, Vol. 233, American Astronomical Society Meeting Abstracts #233, 140.05

Collins, K. A., Kielkopf, J. F., Stassun, K. G., & Hessman, F. V. 2017, *AJ*, 153, 77

Cubillos, P., Erkaev, N. V., Juvan, I., et al. 2017, *MNRAS*, 466, 1868

Cummings, J. D., Deliyannis, C. P., Maderak, R. M., & Steinhauer, A. 2017, *AJ*, 153, 128

Delgado Mena, E., Israeli, G., González Hernández, J. I., et al. 2014, *A&A*, 562, A92

Deline, A., Hooton, M. J., Lendl, M., et al. 2022, *A&A*, 659, A74

Delrez, L., Ehrenreich, D., Alibert, Y., et al. 2021, *Nature Astronomy*, 5, 775

Dorn, C., Khan, A., Heng, K., et al. 2015, *A&A*, 577, A83

Dorn, C. & Lichtenberg, T. 2021, *The Astrophysical Journal Letters*, 922, L4

Dorn, C., Venturini, J., Khan, A., et al. 2017, *Astronomy and Astrophysics*, 597, A37

Doyle, L. R., Wilcox, T. J., & Lorre, J. J. 1984, *ApJ*, 287, 307

Dragomir, D., Teske, J., Günther, M. N., et al. 2019, *ApJ*, 875, L7

Dransfield, G., Mékarnia, D., Triaud, A. H. M. J., et al. 2022, in *Society of Photo-Optical Instrumentation Engineers (SPIE) Conference Series*, Vol. 12186, *Observatory Operations: Strategies, Processes, and Systems IX*, ed. D. S. Adler, R. L. Seaman, & C. R. Benn, 121861F

Espinosa, N., Kossakowski, D., & Brahm, R. 2019, *MNRAS*, 490, 2262

Fausnaugh, M. M., Burke, C. J., Ricker, G. R., & Vanderspek, R. 2020, *Research Notes of the AAS*, 4, 251

Feroz, F., Hobson, M. P., & Bridges, M. 2009, *MNRAS*, 398, 1601

Foreman-Mackey, D., Agol, E., Ambikasaran, S., & Angus, R. 2017, *AJ*, 154, 220

Foreman-Mackey, D., Hogg, D. W., Lang, D., & Goodman, J. 2013, *PASP*, 125, 306

Fossati, L., Erkaev, N. V., Lammer, H., et al. 2017, *A&A*, 598, A90

Fulton, B. J., Petigura, E. A., Blunt, S., & Sinukoff, E. 2018, *PASP*, 130, 044504

Fulton, B. J., Petigura, E. A., Howard, A. W., et al. 2017, *AJ*, 154, 109

Gaia Collaboration, Brown, A. G. A., Vallenari, A., et al. 2021, *A&A*, 649, A1

Gaia Collaboration, Vallenari, A., Brown, A. G. A., et al. 2022, arXiv e-prints, arXiv:2208.00211

Garai, Z., Osborn, H. P., Gandolfi, D., et al. 2023, *A&A*, 674, A44

Gardner, J. P., Mather, J. C., Abbott, R., et al. 2023, *PASP*, 135, 068001

Ginzburg, S., Schlüting, H. E., & Sari, R. 2018, *MNRAS*, 476, 759

Gorti, U., Liseau, R., Sándor, Z., & Clarke, C. 2016, *Space Sci. Rev.*, 205, 125

Guerrero, N. M., Seager, S., Huang, C. X., et al. 2021, *ApJS*, 254, 39

Guillot, T., Abe, L., Agabi, A., et al. 2015, *Astronomische Nachrichten*, 336, 638

Gupta, A. & Schlüting, H. E. 2019, *MNRAS*, 487, 24

Hadden, S. & Lithwick, Y. 2017, *AJ*, 154, 5

Hakim, K., Rivoldini, A., Van Hoolst, T., et al. 2018, in *EGU General Assembly Conference Abstracts*, EGU General Assembly Conference Abstracts, 15447

Helled, R. & Stevenson, D. 2017, *ApJ*, 840, L4

Henry, T. J., Soderblom, D. R., Donahue, R. A., & Baliunas, S. L. 1996, *AJ*, 111, 439

Høg, E., Fabricius, C., Makarov, V. V., et al. 2000, *A&A*, 355, L27

Hoyer, S., Guterman, P., Demangeon, O., et al. 2020, *A&A*, 635, A24

Huang, C. X., Vanderburg, A., Pál, A., et al. 2020, *Research Notes of the American Astronomical Society*, 4, 206

Ikoma, M. & Horii, Y. 2012, *ApJ*, 753, 66

Inamdar, N. K. & Schlüting, H. E. 2015, *MNRAS*, 448, 1751

Jenkins, J. M. 2002, *ApJ*, 575, 493

Jenkins, J. M., Chandrasekaran, H., McCauliff, S. D., et al. 2010, in *Society of Photo-Optical Instrumentation Engineers (SPIE) Conference Series*, Vol. 7740, *Software and Cyberinfrastructure for Astronomy*, ed. N. M. Radziwill & A. Bridger, 77400D

Jenkins, J. M., Tenenbaum, P., Seader, S., et al. 2020, *Kepler Data Processing Handbook: Transiting Planet Search*, Kepler Science Document KSCI-19081-003

Jenkins, J. M., Twicken, J. D., McCauliff, S., et al. 2016, in *Proc. SPIE*, Vol. 9913, *Software and Cyberinfrastructure for Astronomy IV*, 9913E

Jensen, E. 2013, *Tapir: A web interface for transit/eclipse observability*, *Astrophysics Source Code Library*

Jin, S. & Mordasini, C. 2018, *ApJ*, 853, 163

Johnstone, C. P., Güdel, M., Brott, I., & Lüftinger, T. 2015a, *A&A*, 577, A28

Johnstone, C. P., Güdel, M., Stökl, A., et al. 2015b, *ApJ*, 815, L12

Kempton, E. M. R., Bean, J. L., Louie, D. R., et al. 2018, *PASP*, 130, 114401

Kimura, S. S., Kunitomo, M., & Takahashi, S. Z. 2016, *MNRAS*, 461, 2257

Kreidberg, L. 2015, *PASP*, 127, 1161

Krenn, A. F., Lendl, M., Patel, J. A., et al. 2023, *A&A*, 672, A24

Kubyshkina, D., Cubillos, P. E., Fossati, L., et al. 2019a, *ApJ*, 879, 26

Kubyshkina, D., Fossati, L., Erkaev, N. V., et al. 2018, *A&A*, 619, A151

Kubyshkina, D., Fossati, L., Mustill, A. J., et al. 2019b, *A&A*, 632, A65

Kurucz, R. 1993a, *SYNTHE Spectrum Synthesis Programs and Line Data*. Kurucz CD-ROM No. 18. Cambridge, 18

Kurucz, R. L. 1993b, *SYNTHE spectrum synthesis programs and line data (Astrophysics Source Code Library)*

Lee, E. J. & Chiang, E. 2015, *ApJ*, 811, 41

Lee, E. J., Karalis, A., & Thorngren, D. P. 2022, *ApJ*, 941, 186

Leleu, A., Alibert, Y., Hara, N. C., et al. 2021, *Astronomy and Astrophysics*, 649, A26

Lendl, M., Bouchy, F., Gill, S., et al. 2020, *MNRAS*, 492, 1761

Li, J., Tenenbaum, P., Twicken, J. D., et al. 2019, *PASP*, 131, 024506

Lindgren, L., Bastian, U., Biermann, M., et al. 2021, *A&A*, 649, A4

Lopez, E. D. & Fortney, J. J. 2013, *ApJ*, 776, 2

Lozovsky, M., Helled, R., Dorn, C., & Venturini, J. 2018, *ApJ*, 866, 49

Lucy, L. B. & Sweeney, M. A. 1971, AJ, 76, 544

Luque, R., Nowak, G., Pallé, E., et al. 2019, A&A, 623, A114

Maciel, W. J., Rodrigues, T. S., & Costa, R. D. D. 2011, A&A, 47, 401

Marcy, G. W., Isaacson, H., Howard, A. W., et al. 2014, ApJS, 210, 20

Marigo, P., Girardi, L., Bressan, A., et al. 2017, ApJ, 835, 77

Masuda, K. & Winn, J. N. 2020, AJ, 159, 81

Maxted, P. F. L., Ehrenreich, D., Wilson, T. G., et al. 2022, MNRAS, 514, 77

McCullly, C., Volgenau, N. H., Harbeck, D.-R., et al. 2018, in Society of Photo-Optical Instrumentation Engineers (SPIE) Conference Series, Vol. 10707, Proc. SPIE, 107070K

McLaughlin, D. B. 1924, ApJ, 60, 22

Mékarnia, D., Guillot, T., Rivet, J. P., et al. 2016, MNRAS, 463, 45

Millholland, S., Wang, S., & Laughlin, G. 2017, ApJ, 849, L33

Mishra, L., Alibert, Y., Udry, S., & Mordasini, C. 2023, A&A, 670, A68

Mol Lous, M., Helled, R., & Mordasini, C. 2022, Nature Astronomy, 6, 819

Mordasini, C. 2020, A&A, 638, A52

Morris, R. L., Twicken, J. D., Smith, J. C., et al. 2020, Kepler Data Processing Handbook: Photometric Analysis, Kepler Science Document KSCI-19081-003

Naponiello, L., Mancini, L., Sozzetti, A., et al. 2023, arXiv e-prints, arXiv:2309.01464

Nordström, B., Mayor, M., Andersen, J., et al. 2004, A&A, 418, 989

Osborn, H. P. 2022, MonoTools: Planets of uncertain periods detector and modeler, Astrophysics Source Code Library, record ascl:2204.020

Osborn, H. P., Nowak, G., Hébrard, G., et al. 2023, MNRAS, 523, 3069

Otegi, J. F., Bouchy, F., & Helled, R. 2020, A&A, 634, A43

Otegi, J. F., Helled, R., & Bouchy, F. 2022, A&A, 658, A107

Owen, J. E. & Wu, Y. 2017, ApJ, 847, 29

Pepe, F., Cristiani, S., Rebolo, R., et al. 2021, A&A, 645, A96

Petigura, E. A., Rogers, J. G., Isaacson, H., et al. 2022, AJ, 163, 179

Pollacco, D. L., Skillen, I., Collier Cameron, A., et al. 2006, PASP, 118, 1407

Ricker, G. R., Winn, J. N., Vanderspek, R., et al. 2015, Journal of Astronomical Telescopes, Instruments, and Systems, 1, 014003

Rogers, J. G. & Owen, J. E. 2021, MNRAS, 503, 1526

Rossiter, R. A. 1924, ApJ, 60, 15

Santos, N. C., Sousa, S. G., Mortier, A., et al. 2013, A&A, 556, A150

Schanche, N., Hébrard, G., Collier Cameron, A., et al. 2020, MNRAS, 499, 428

Schmider, F.-X., Abe, L., Agabi, A., et al. 2022, in Society of Photo-Optical Instrumentation Engineers (SPIE) Conference Series, Vol. 12182, Ground-based and Airborne Telescopes IX, ed. H. K. Marshall, J. Spyromilio, & T. Usuda, 121822O

Sestito, P. & Randich, S. 2005, A&A, 442, 615

Skrutskie, M. F., Cutri, R. M., Stiening, R., et al. 2006, AJ, 131, 1163

Smith, J. C., Stumpe, M. C., Van Cleve, J. E., et al. 2012, PASP, 124, 1000

Sneden, C. A. 1973, PhD thesis, THE UNIVERSITY OF TEXAS AT AUSTIN.

Sousa, S. G. 2014, [arXiv:1407.5817] [arXiv:1407.5817]

Sousa, S. G., Adibekyan, V., Delgado-Mena, E., et al. 2021, A&A, 656, A53

Sousa, S. G., Santos, N. C., Adibekyan, V., Delgado-Mena, E., & Israeli, G. 2015, A&A, 577, A67

Sousa, S. G., Santos, N. C., Israeli, G., Mayor, M., & Monteiro, M. J. P. F. G. 2007, A&A, 469, 783

Sousa, S. G., Santos, N. C., Mayor, M., et al. 2008, A&A, 487, 373

Speagle, J. S. 2020, MNRAS, 493, 3132

Stassun, K. G., Oelkers, R. J., Paegert, M., et al. 2019, AJ, 158, 138

Stumpe, M. C., Smith, J. C., Catanzarite, J. H., et al. 2014, PASP, 126, 100

Stumpe, M. C., Smith, J. C., Van Cleve, J. E., et al. 2012, PASP, 124, 985

Sun, L., Ioannidis, P., Gu, S., et al. 2019, A&A, 624, A15

Sun, Q., Deliyannis, C. P., Steinhauer, A., Anthony-Twarog, B. J., & Twarog, B. A. 2023, ApJ, 952, 71

Tokovinin, A. 2018, PASP, 130, 035002

Tsantaki, M., Sousa, S. G., Adibekyan, V. Z., et al. 2013, A&A, 555, A150

Tu, L., Johnstone, C. P., Güdel, M., & Lammer, H. 2015, A&A, 577, L3

Twicken, J. D., Catanzarite, J. H., Clarke, B. D., et al. 2018, PASP, 130, 064502

Twicken, J. D., Clarke, B. D., Bryson, S. T., et al. 2010, in Proc. SPIE, Vol. 7740, Software and Cyberinfrastructure for Astronomy, 774023

Ulmer-Moll, S., Osborn, H. P., Tuson, A., et al. 2023, A&A, 674, A43

Vanderburg, A. & Johnson, J. A. 2014, PASP, 126, 948

Venturini, J., Guilera, O. M., Haldemann, J., Ronco, M. P., & Mordasini, C. 2020, A&A, 643, L1

Venturini, J. & Helled, R. 2017, ApJ, 848, 95

Weiss, L. M., Marcy, G. W., Petigura, E. A., et al. 2018, AJ, 155, 48

Wielen, R. 1977, A&A, 60, 263

Winn, J. N. 2010, arXiv e-prints, arXiv:1001.2010

Winn, J. N., Holman, M. J., Henry, G. W., et al. 2007, AJ, 133, 1828

Wright, E. L., Eisenhardt, P. R. M., Mainzer, A. K., et al. 2010, AJ, 140, 1868

Zechmeister, M. & Kürster, M. 2009, A&A, 496, 577

Zeng, L., Sasselov, D. D., & Jacobsen, S. B. 2016, ApJ, 819, 127

Ziegler, C., Tokovinin, A., Briceno, C., et al. 2020, VizieR Online Data Catalog, J/AJ/159/19

¹ Observatoire de Genève, Université de Genève, Chemin Pegasi, 51, 1290 Versoix, Switzerland

² Center for Space and Habitability, University of Bern, Gesellschaftsstrasse 6, 3012 Bern, Switzerland

³ Department of Physics and Kavli Institute for Astrophysics and Space Research, Massachusetts Institute of Technology, Cambridge, MA 02139, USA

⁴ Weltraumforschung und Planetologie, Physikalisches Institut, University of Bern, Gesellschaftsstrasse 6, 3012 Bern, Switzerland

⁵ Instituto de Astrofísica e Ciências do Espaço, Universidade do Porto, CAUP, Rua das Estrelas, 4150-762 Porto, Portugal

⁶ Departamento de Física e Astronomia, Faculdade de Ciências, Universidade do Porto, Rua do Campo Alegre, 4169-007 Porto, Portugal

⁷ Space Research Institute, Austrian Academy of Sciences, Schmiedlstraße 6, 8042 Graz, Austria

⁸ Center for Astrophysics | Harvard & Smithsonian, 60 Garden Street, Cambridge, MA 02138, USA

⁹ Université Côte d'Azur, Observatoire de la Côte d'Azur, CNRS, Laboratoire Lagrange, Bd de l'Observatoire, CS 34229, 06304 Nice cedex 4, France

¹⁰ Institute for Computational Science, University of Zurich, Winterthurerstr. 90, 8057 Zurich, Switzerland

¹¹ Astrophysics Group, Keele University, Staffordshire ST5 5BG, UK

¹² Department of Astronomy & Astrophysics, University of Chicago, Chicago, IL 60637, USA

¹³ NASA Ames Research Center, Moffett Field, CA 94035, USA

¹⁴ Research Institute for Advanced Computer Science, Universities Space Research Association, Washington, DC 20024, USA

¹⁵ Department of Physics and Astronomy, Union College, 807 Union St., Schenectady, NY 12308, USA

¹⁶ Department of Physics, University of Warwick, Gibbet Hill Road, Coventry CV4 7AL, UK

¹⁷ Department of Astrophysical Sciences, Princeton University, Princeton, NJ 08544, USA

¹⁸ Department of Physics, Engineering and Astronomy, Stephen F. Austin State University, 1936 North St, Nacogdoches, TX 75962, USA

¹⁹ Dipartimento di Fisica e Astronomia "Galileo Galilei", Università degli Studi di Padova, Vicolo dell'Osservatorio 3, 35122 Padova, Italy

²⁰ INAF, Osservatorio Astronomico di Padova, Vicolo dell'Osservatorio 5, 35122 Padova, Italy

²¹ Department of Astronomy, Stockholm University, AlbaNova University Center, 10691 Stockholm, Sweden

²² Dipartimento di Fisica, Università degli Studi di Torino, via Pietro Giuria 1, I-10125, Torino, Italy

²³ Cavendish Laboratory, JJ Thomson Avenue, Cambridge CB3 0HE, UK

²⁴ Institute of Astronomy, University of Cambridge, Madingley Road, Cambridge, CB3 0HA, United Kingdom Département de Physique, Institut Trottier de Recherche sur les Exoplanètes, Université de Montréal, Montréal, Québec, H3T 1J4, Canada

²⁵ Instituto de Astrofísica de Canarias, Via Lactea s/n, 38200 La Laguna, Tenerife, Spain

²⁶ Departamento de Astrofísica, Universidad de La Laguna, Astrofísico Francisco Sanchez s/n, 38206 La Laguna, Tenerife, Spain

²⁷ Institut de Ciències de l'Espai (ICE, CSIC), Campus UAB, Can Magrans s/n, 08193 Bellaterra, Spain

²⁸ Institut d'Estudis Espacials de Catalunya (IEEC), Gran Capità 2-4, 08034 Barcelona, Spain

²⁹ Admatis, 5, Károly Kálmán Street, 3534 Miskolc, Hungary

³⁰ Depto. de Astrofísica, Centro de Astrobiología (CSIC-INTA), ESAC campus, 28692 Villanueva de la Cañada (Madrid), Spain

³¹ Université Grenoble Alpes, CNRS, IPAG, 38000 Grenoble, France

³² Caltech/IPAC-NASA Exoplanet Science Institute, 770 S. Wilson Avenue, Pasadena, CA 91106, USA

³³ Centre for Exoplanet Science, SUPA School of Physics and Astronomy, University of St Andrews, North Haugh, St Andrews KY16 9SS, UK

³⁴ Université de Paris Cité, Institut de physique du globe de Paris,
CNRS, 1 Rue Jussieu, F-75005 Paris, France

³⁵ Institute of Planetary Research, German Aerospace Center (DLR),
Rutherfordstrasse 2, 12489 Berlin, Germany

³⁶ European Southern Observatory, Av. Alonso de Cordova 3107,
Casilla 19001, Santiago de Chile, Chile

³⁷ Centre for Mathematical Sciences, Lund University, Box 118, 221
00 Lund, Sweden

³⁸ Department of Physics and McDonnell Center for the Space Sci-
ences, Washington University, St. Louis, MO 63130, USA

³⁹ Aix Marseille Univ, CNRS, CNES, LAM, 38 rue Frédéric Joliot-
Curie, 13388 Marseille, France

⁴⁰ Astrobiology Research Unit, Université de Liège, Allée du 6 Août
19C, B-4000 Liège, Belgium

⁴¹ Space sciences, Technologies and Astrophysics Research (STAR)
Institute, Université de Liège, Allée du 6 Août 19C, 4000 Liège,
Belgium

⁴² ETH Zurich, Institute for Particle Physics and Astrophysics,
Wolfgang-Pauli-Strasse 27, CH-8093 Zurich Switzerland

⁴³ Institut d'astrophysique de Paris, UMR7095 CNRS, Université
Pierre & Marie Curie, 98bis Blvd. Arago, 75014 Paris, France

⁴⁴ Airbus Defence and Space SAU, C/ Aviocar 2, 28906 Getafe,
Madrid, Spain

⁴⁵ Leiden Observatory, University of Leiden, PO Box 9513, 2300 RA
Leiden, The Netherlands

⁴⁶ Department of Space, Earth and Environment, Chalmers University
of Technology, Onsala Space Observatory, 439 92 Onsala, Sweden

⁴⁷ Department of Astrophysics, University of Vienna, Türkenschanz-
trasse 17, 1180 Vienna, Austria

⁴⁸ European Space Agency (ESA), European Space Research and
Technology Centre (ESTEC), Keplerlaan 1, 2201 AZ Noordwijk,
The Netherlands

⁴⁹ Institute for Theoretical Physics and Computational Physics, Graz
University of Technology, Petersgasse 16, 8010 Graz, Austria

⁵⁰ Konkoly Observatory, Research Centre for Astronomy and Earth
Sciences, 1121 Budapest, Konkoly Thege Miklós út 15-17, Hungary

⁵¹ ELTE Eötvös Loránd University, Institute of Physics, Pázmány Péter
sétány 1/A, 1117 Budapest, Hungary

⁵² IMCCE, UMR8028 CNRS, Observatoire de Paris, PSL Univ., Sor-
bonne Univ., 77 av. Denfert-Rochereau, 75014 Paris, France

⁵³ Proto-Logic LLC, 1718 Euclid Street NW, Washington, DC 20009,
USA

⁵⁴ European Southern Observatory, Karl-Schwarzschild-Straße 2,
85748 Garching bei München, Germany

⁵⁵ INAF Osservatorio Astrofisico di Catania, via S. Sofia 78, 95123
Catania, Italy

⁵⁶ Zentrum für Astronomie und Astrophysik, Technische Universität
Berlin, Hardenbergstr. 36, D-10623 Berlin, Germany

⁵⁷ Institut fuer Geologische Wissenschaften, Freie Universität Berlin,
Malteserstrasse 74-100, 12249 Berlin, Germany

⁵⁸ Department of Earth, Atmospheric and Planetary Sciences, Mas-
sachusetts Institute of Technology, Cambridge, MA 02139, USA

⁵⁹ Department of Aeronautics and Astronautics, MIT, 77 Mas-
sachusetts Avenue, Cambridge, MA 02139, USA

⁶⁰ ELTE Eötvös Loránd University, Gothard Astrophysical Observa-
tory, 9700 Szombathely, Szent Imre h. u. 112, Hungary

⁶¹ HUN-REN-ELTE Exoplanet Research Group, Szent Imre h. u. 112.,
Szombathely, H-9700, Hungary

⁶² NASA Goddard Space Flight Center, 8800 Greenbelt Road, Green-
belt, MD 20771, USA

⁶³ Centre for Exoplanets and Habitability, University of Warwick, Gib-
bet Hill Road, Coventry CV4 7AL, UK

Appendix A: TESS light curves

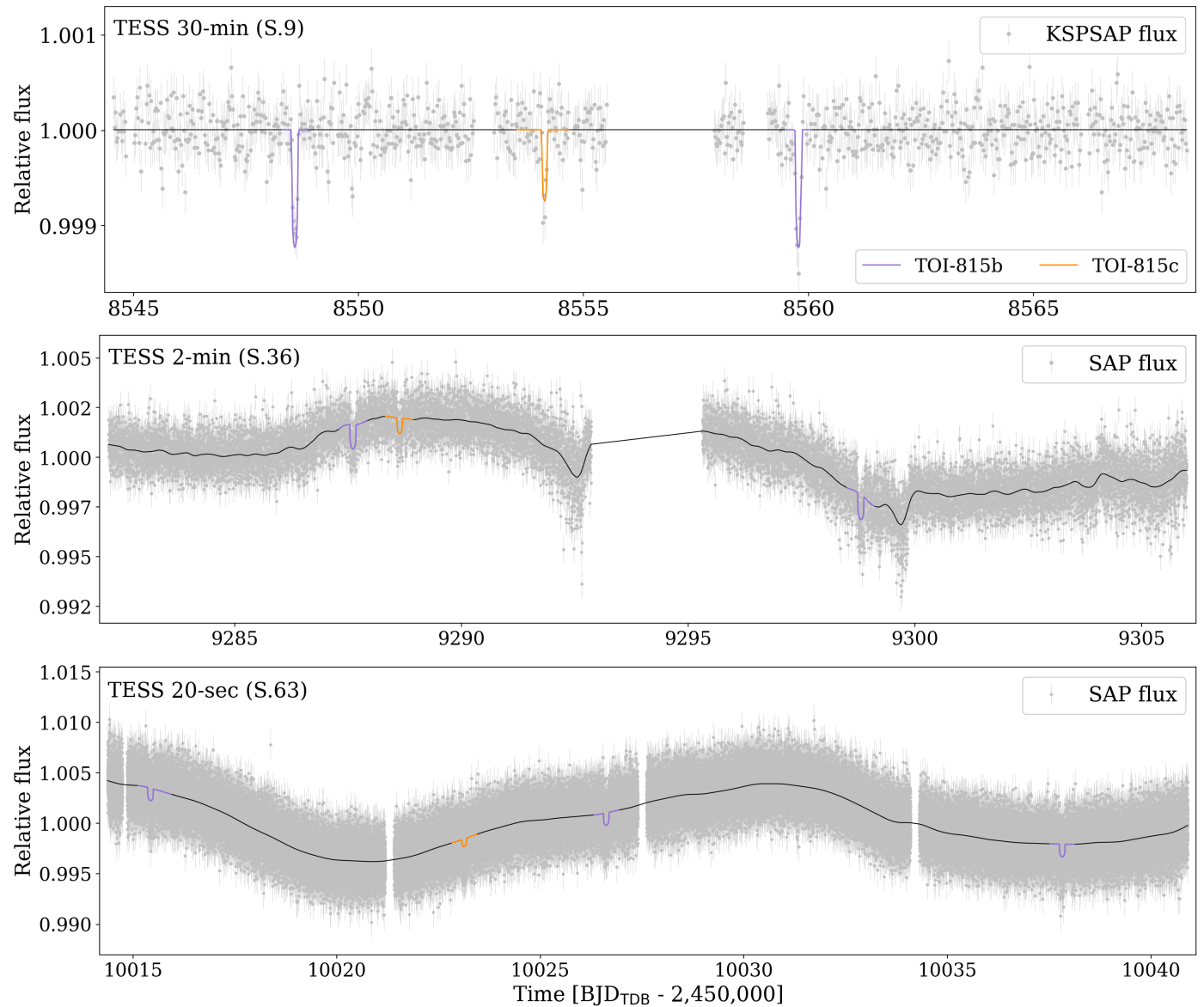


Fig. A.1: TESS SAP flux light curves with the best-fit juliet model shown with the black line (see Sect. 4 for details on the modeling). The transits of TOI-815b and TOI-815c are indicated with purple and orange, respectively.

Appendix B: RVs with ESPRESSO

Table B.1: ESPRESSO RV observations for TOI-815, along with activity indicator measurements, i.e. FWHM, bisector, and $\log R'_{HK}$.

Time [BJD-2 450 000]	RV [m s ⁻¹]	σ_{RV} [m s ⁻¹]	FWHM ⁽²⁾ [m s ⁻¹]	BIS ⁽²⁾	$\log R'_{HK}$ ⁽³⁾	t _{exp} [s]
9308.60433	-2973.3950	0.6145	6474.143	-33.038	-4.7084	600
9310.60679	-2970.1704	0.7233	6470.941	-33.052	-4.7338	600
9313.73506 ⁽¹⁾	-2962.6373	0.5712	6492.966	-30.291	-4.6757	600
9316.52823	-2967.0427	0.7459	6494.718	-23.625	-4.7107	600
9318.53033	-2968.9726	0.5863	6478.690	-29.060	-4.6762	600
9324.54484	-2979.7547	0.8117	6513.799	-28.181	-4.6859	600
9327.50777 ⁽¹⁾	-2965.7154	0.4397	6482.962	-32.938	-4.6229	600
9329.52592 ⁽¹⁾	-2971.0105	0.9842	6543.347	-29.283	-4.7529	600
9332.57219	-2979.7266	0.6474	6491.382	-26.738	-4.6824	600
9336.49956 ⁽¹⁾	-2982.4246	1.3115	6515.936	-40.000	-4.9931	600
9339.48187	-2973.6498	0.5988	6468.715	-33.267	-4.7189	600
9341.51194 ⁽¹⁾	-2966.5835	0.9108	6513.090	-35.131	-4.7516	600
9346.54064	-2972.2321	0.5959	6482.420	-24.888	-4.6930	600
9373.49668	-2973.5189	0.5467	6462.905	-33.991	-4.6367	600
9375.51475	-2971.6794	0.6513	6471.909	-32.600	-4.6265	600
9406.50596	-2975.2108	0.7212	6492.234	-32.504	-4.6149	600
9410.48054	-2971.8872	0.6759	6499.208	-30.202	-4.6978	600
9415.50797	-2971.5355	0.8107	6491.252	-26.700	-4.6620	600
9673.54348	-2977.4158	0.5684	6488.390	-34.257	-4.6894	700
9675.51515	-2973.7947	0.9406	6487.917	-25.694	-4.6418	700
9677.65231	-2972.6960	0.8151	6492.405	-31.643	-4.6580	700
9679.55323 ⁽¹⁾	-2973.4334	0.5445	6497.504	-32.766	-4.6080	700
9683.53185	-2981.6090	0.4694	6497.328	-29.483	-4.6329	700
9685.55122	-2980.4065	0.7458	6496.394	-24.517	-4.6203	700
9687.52944	-2972.0070	0.4487	6495.493	-29.672	-4.6432	700
9695.52289	-2967.3200	0.9486	6512.740	-29.566	-4.7299	700
9697.58163	-2965.9727	0.5759	6511.966	-26.858	-4.6611	700
9784.49262	-2977.5647	0.6128	6525.410	-22.486	-4.6248	700
9904.83330	-2969.5919	0.4342	6487.460	-35.249	-4.6440	700
9905.77809	-2970.1154	0.6533	6491.720	-34.630	-4.6797	700
9906.80910	-2970.1976	0.4551	6492.162	-33.028	-4.6399	700
9907.79772	-2969.7455	1.3028	6534.337	-38.113	-4.8075	700
9910.75047	-2966.0686	0.7246	6503.361	-25.248	-4.6902	700
9917.72905	-2978.0604	0.6064	6481.170	-33.996	-4.6673	700

Notes:

⁽¹⁾ These data did not pass the ESPRESSO flux quality control and therefore were excluded from the analysis.

⁽²⁾ The uncertainties of FWHM and BIS are twice the uncertainties of the RVs ($2\sigma_{RV}$).

⁽³⁾ The median uncertainty of $\log R'_{HK}$ is 0.03.

Appendix C: Spectral synthesis

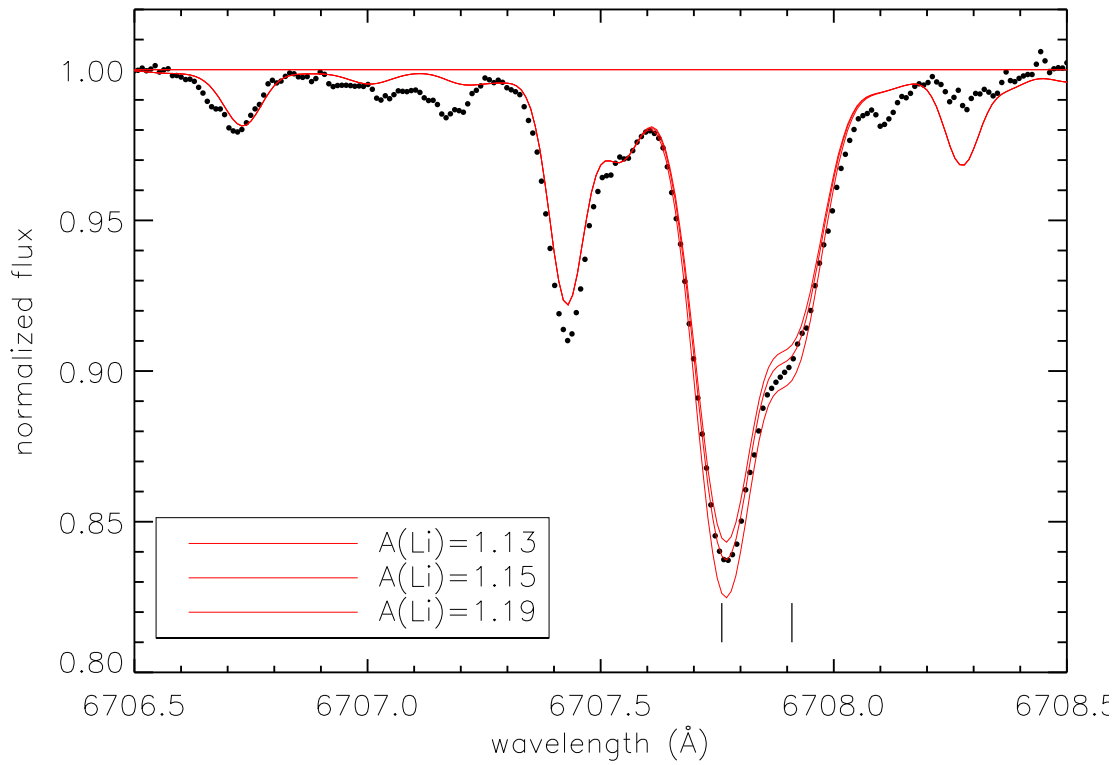


Fig. C.1: Spectral synthesis around the Li doublet. The vertical lines mark the position of the lines.

Appendix D: Generalized Lomb-Scargle periodograms

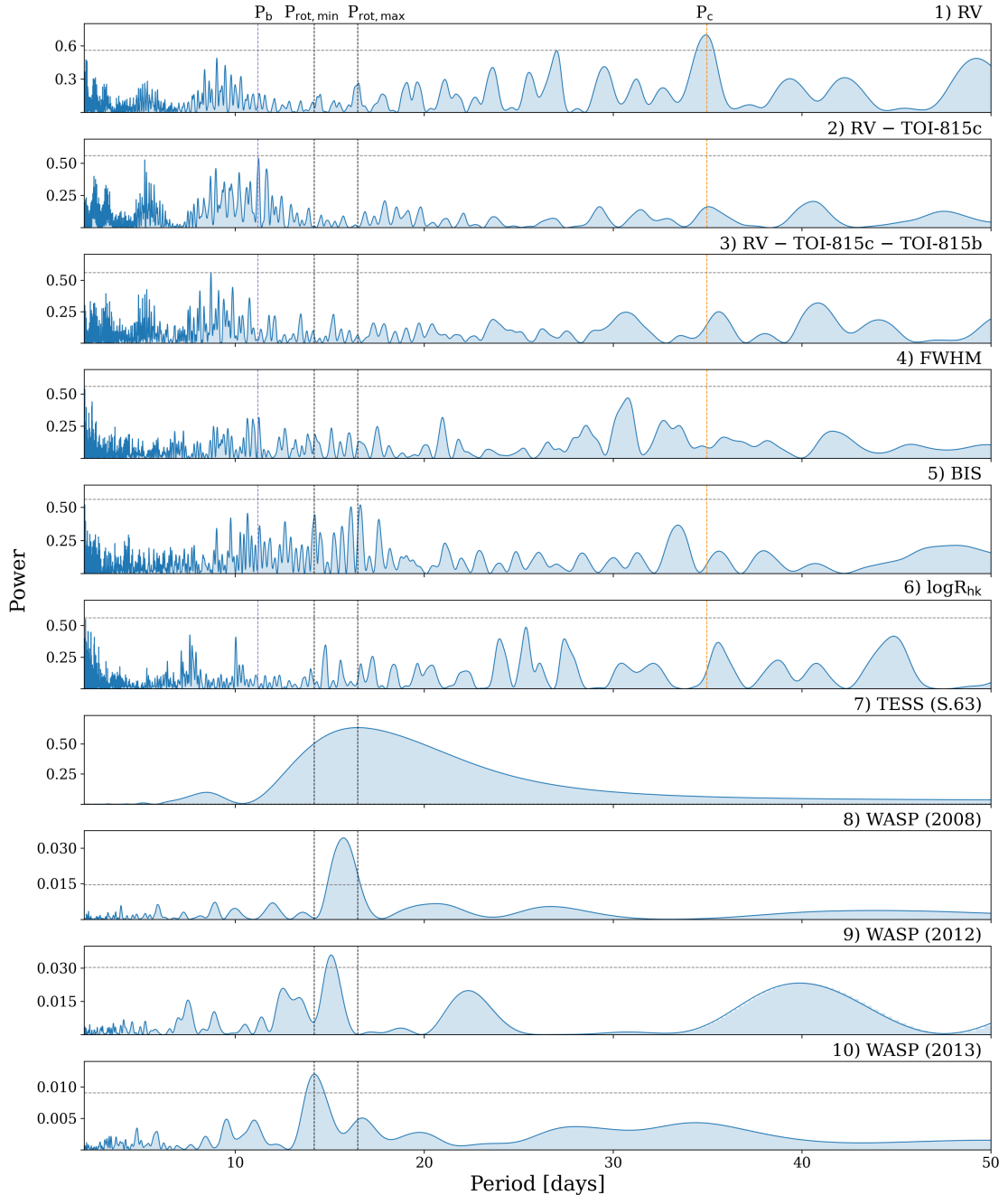


Fig. D.1: Generalized Lomb-Scargle periodogram of the TOI-815 spectroscopic and photometric time series. More specifically: 1) RV ESPRESSO measurements, 2) RV residuals, after the subtraction of TOI-815c signal, 2) RV residuals, after the subtraction of TOI-815b and c signals, 3-5) FWHM, bisector and Ca II H & K line activity indicator ($\log R'_{HK}$), 7) TESS Sector 63 photometric data, 8-10) WASP photometric data (2008, 2012 and 2023). The two black vertical lines correspond to the minimum and maximum rotation periods ($P_{rot,min} \sim 14.2$ days and $P_{rot,max} \sim 16.5$ days). The purple and orange vertical lines correspond to the orbital periods of planets b ($P_b \sim 11.2$ days) and c ($P_c \sim 35$ days), respectively. The gray horizontal lines indicating the 1% false alarm probability (FAP).

Appendix E: Priors

Table E.1: Maximum values and 68% confidence intervals of the posterior distributions from joint modeling with `juliet`.

Parameter	Prior ^(a)	Value ^(b)
Jump stellar parameters		
Stellar density, ρ_* (ρ_\odot)	$\mathcal{N}(2396, 139)$	2431_{-125}^{+122}
Jump parameters for TOI-815b		
Orbital period, P_{orb} (days)	$\mathcal{U}(10, 12)$	$11.197259_{-0.000017}^{+0.000018}$
Transit epoch, T_0 (BJD)	$\mathcal{N}(2459287.6, 0.1)$	$2459287.6028_{-0.0009}^{+0.0009}$
Scaled planetary radius, R_P/R_*	$\mathcal{U}(0, 1)$	$0.0349_{-0.0004}^{+0.0004}$
Impact parameter, b	$\mathcal{U}(0, 1)$	$0.279_{-0.073}^{+0.058}$
Eccentricity, e	$\mathcal{F}(0)$	0 (adopted, $3\sigma < 0.20$)
Argument of periastron, ω_* (deg)	$\mathcal{F}(90)$	-
Radial velocity semi-amplitude, K (m s ⁻¹)	$\mathcal{U}(0, 100)$	$2.6_{-0.5}^{+0.5}$
Jump parameters for TOI-815c		
Orbital period, P_{orb} (days)	$\mathcal{U}(34, 36)$	$34.976145_{-0.000097}^{+0.000099}$
Transit epoch, T_0 (BJD)	$\mathcal{N}(2459288.6, 0.1)$	$2459288.6331_{-0.0024}^{+0.0023}$
Scaled planetary radius, R_P/R_*	$\mathcal{U}(0, 1)$	$0.0312_{-0.0010}^{+0.0011}$
Impact parameter, b	$\mathcal{U}(0, 1)$	$0.839_{-0.016}^{+0.015}$
Eccentricity, e	$\mathcal{F}(0)$	0 (adopted, $3\sigma < 0.22$)
Argument of periastron, ω_* (deg)	$\mathcal{F}(90)$	-
Radial velocity semi-amplitude, K (m s ⁻¹)	$\mathcal{U}(0, 100)$	$5.5_{-0.5}^{+0.5}$
Instrumental photometric parameters		
Offset relative flux, $M_{TESS_{S9}}$ (10^{-6})	$\mathcal{N}(0, 0.1)$	$-8.6_{-8.2}^{+8.0}$
Jitter, $\sigma_{w,TESS_{S9}}$ (ppm)	$\log\mathcal{U}(0.01, 1000)$	$0.5_{-0.5}^{+6.5}$
Offset relative flux, $M_{TESS_{S36}}$ (10^{-6})	$\mathcal{N}(0, 0.1)$	-72_{-417}^{+411}
Jitter, $\sigma_{w,TESS_{S36}}$ (ppm)	$\log\mathcal{U}(0.01, 1000)$	466_{-8}^{+8}
Offset relative flux, $M_{TESS_{S63}}$ (10^{-6})	$\mathcal{N}(0, 0.1)$	-3594_{-6137}^{+3821}
Jitter, $\sigma_{w,TESS_{S63}}$ (ppm)	$\log\mathcal{U}(0.01, 1000)$	457_{-1}^{+11}
Offset relative flux, M_{CHEOPS_1} (10^{-6})	$\mathcal{N}(0, 0.1)$	-197_{-44}^{+46}
Jitter, $\sigma_{w,CHEOPS_1}$ (ppm)	$\log\mathcal{U}(0.01, 1000)$	299_{-22}^{+23}
Offset relative flux, M_{CHEOPS_2} (10^{-6})	$\mathcal{N}(0, 0.1)$	-474_{-48}^{+48}
Jitter, $\sigma_{w,CHEOPS_2}$ (ppm)	$\log\mathcal{U}(0.01, 1000)$	404_{-23}^{+24}
Offset relative flux, M_{CHEOPS_3} (10^{-6})	$\mathcal{N}(0, 0.1)$	-322_{-35}^{+34}
Jitter, $\sigma_{w,CHEOPS_3}$ (ppm)	$\log\mathcal{U}(0.01, 1000)$	293_{-19}^{+19}
Offset relative flux, M_{LCO} (10^{-6})	$\mathcal{N}(0, 0.1)$	1089_{-88}^{+88}
Jitter, $\sigma_{w,LCO}$ (ppm)	$\log\mathcal{U}(0.01, 5000)$	986_{-68}^{+72}
Offset relative flux, M_{ASTEP} (10^{-6})	$\mathcal{N}(0, 0.1)$	761_{-131}^{+133}
Jitter, $\sigma_{w,ASTEP}$ (ppm)	$\log\mathcal{U}(0.01, 5000)$	3369_{-85}^{+89}
GP parameters		
$\sigma_{GP,TESS_{S9}}$ (relative flux)	$\mathcal{F}(0)$	-
$\rho_{GP,TESS_{S9}}$ (days)	$\mathcal{F}(0)$	-
$\sigma_{GP,TESS_{S36}}$ (10^{-4} relative flux)	$\log\mathcal{U}(10^{-6}, 100)$	12_{-2}^{+2}
$\rho_{GP,TESS_{S36}}$ (days)	$\log\mathcal{U}(0.001, 100)$	$0.94_{-0.11}^{+0.13}$
$\sigma_{GP,TESS_{S63}}$ (10^{-4} relative flux)	$\log\mathcal{U}(10^{-6}, 100)$	57_{-22}^{+44}
$\rho_{GP,TESS_{S63}}$ (days)	$\log\mathcal{U}(0.001, 100)$	$9.11_{-2.77}^{+4.37}$
Instrumental RV parameters		
Jitter, $\sigma_{w,ESPRESSO}$ (m s ⁻¹)	$\log\mathcal{U}(0.001, 100)$	$1.88_{-0.25}^{+0.29}$
Systemic RV, $\mu_{ESPRESSO}$ (m s ⁻¹)	$\mathcal{U}(-3500, -1000)$	$-2973.61_{-0.36}^{+0.36}$
Limb darkening parameters		
$q_{1,ESPRESSO}$	$\mathcal{N}(0.408, 0.017)$	$0.407_{-0.007}^{+0.015}$
$q_{2,ESPRESSO}$	$\mathcal{N}(0.349, 0.022)$	$0.343_{-0.015}^{+0.020}$
$q_{1,CHEOPS}$	$\mathcal{N}(0.519, 0.012)$	$0.518_{-0.011}^{+0.019}$
$q_{2,CHEOPS}$	$\mathcal{N}(0.408, 0.012)$	$0.406_{-0.011}^{+0.011}$
$q_{1,LCO}$	$\mathcal{N}(0.324, 0.008)$	$0.324_{-0.007}^{+0.007}$
$q_{2,LCO}$	$\mathcal{N}(0.314, 0.014)$	$0.314_{-0.012}^{+0.012}$
$q_{1,ASTEP}$	$\mathcal{N}(0.492, 0.016)$	$0.492_{-0.014}^{+0.014}$
$q_{2,ASTEP}$	$\mathcal{N}(0.376, 0.017)$	$0.378_{-0.016}^{+0.015}$

Notes: ^(a)For the priors, $\mathcal{N}(\mu, \sigma^2)$ indicates a normal distribution with mean μ and variance σ^2 , $\mathcal{U}(a, b)$ a uniform distribution between a and b , $\log\mathcal{U}(a, b)$ a log-uniform distribution between a and b and $\mathcal{F}(a)$ a parameter fixed to value a . ^(b)The posterior estimate indicates the median value and then error bars for the 68 % credibility intervals.

Appendix F: CHEOPS alias hunting

Table F.1: CHEOPS photometric observations of TOI-815.

Visit	Expected planet	Start time [UTC]	Duration [h]	Eff. [%]	RMS ppm	Alias	Detection	File key	Detrending ^(d)
1	c	2022-03-06 00:36	8.34	73	422	22.26	no	CH_PR110048_TG018001_V0300	(e)
2	c	2022-03-06 16:26	8.37	60	461	20.99	no	CH_PR110048_TG018901_V0300	(e)
3	c	2022-03-17 04:35	9.84	61	417	22.95	no	CH_PR110048_TG018101_V0300	(e)
4 ^(a)	b	2022-03-18 08:36	11.64	66	514	11.20	yes	CH_PR100031_TG050801_V0300	t, x, y, y ² , sin(ϕ), cos(ϕ), cos(2 ϕ)
5	c	2022-04-13 01:20	8.47	60	429	17.92	no	CH_PR110048_TG025201_V0300	(e)
6	c	2022-04-30 06:47	8.34	51	497	29.38	no	CH_PR110048_TG027601_V0300	t (clear flux trend in data)
7	c	2023-02-15 11:09	8.29	69	520	31.93	no	CH_PR110048_TG036501_V0300	(e)
8	c	2023-02-22 01:40	9.04	68	447	25.33	no	CH_PR110048_TG036701_V0300	(e)
9	c	2023-02-27 14:48	8.22	64	580	19.85	no	CH_PR110048_TG036901_V0300	(e)
10 ^(b)	b	2023-02-28 14:16	8.39	62	460	18.83	yes	CH_PR110048_TG037001_V0300	t ² , x, y, y ² , bg, sin(ϕ), sin(2 ϕ), cos(2 ϕ)
11 ^(c)	c	2023-04-23 08:31	10.09	58	462	34.98	yes	CH_PR110048_TG042201_V0300	t, t ² , y, y ² , bg, cos(ϕ)

Notes:

(a) Figure 7, left.

(b) Figure 7, center.

(c) Figure 7, right.

(d) The correlation terms were determined using `pycheops`.

(e) Detrended with: x, y, bg, cos(ϕ), sin(ϕ), sin(2 ϕ), sin(3 ϕ), ΔT , sin(ϕ), sin(2 ϕ), sin(3 ϕ), bg², x², y²

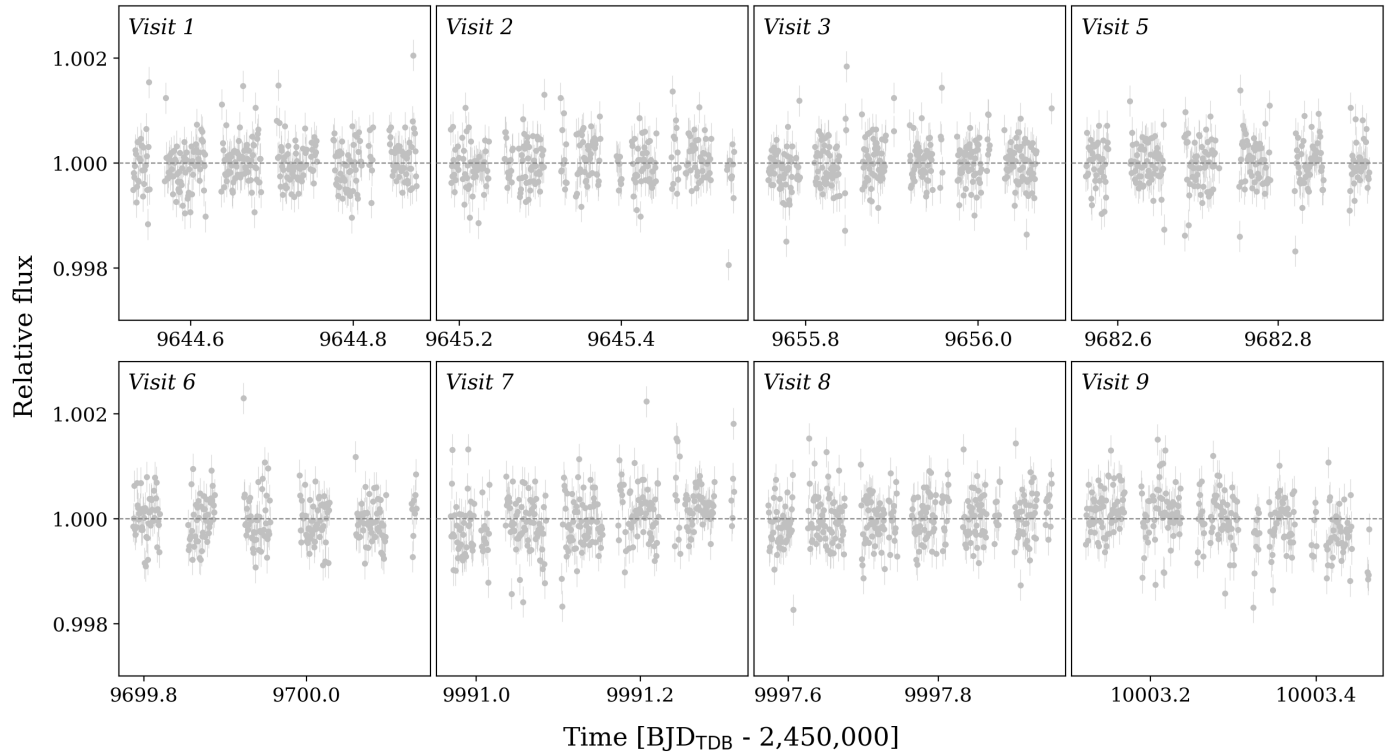


Fig. F.1: CHEOPS unsuccessful transit observations that ruled out the most-likely period aliases of TOI-815c. The data have been detrended using the detrending terms presented in Table F.1.